Investigating the local atmospheric response to a realistic shift in the Oyashio sea surface temperature front

Dimitry Smirnov* and Matthew Newman
CIRES, University of Colorado at Boulder, and NOAA/ESRL, Boulder, Colorado

Michael A. Alexander
NOAA/ESRL, Boulder, Colorado

Young-Oh Kwon
WHOI, Woods Hole, Massachusetts

Claude Frankignoul
LOCEAN/IPSL, Université Pierre et Marie Curie, Paris, France

* *Corresponding author address:* Dimitry Smirnov, NOAA/ESRL, 325 Broadway, R/PSD1, Boulder, CO 80305.
E-mail: chillwx@gmail.com

Abstract

The local atmospheric response to a realistic shift of the Oyashio Extension SST front in the western North Pacific is analyzed using a high-resolution (0.25°, HR) version of the global Community Atmosphere Model version 5 (CAM5). A northward shift in the SST front causes an atmospheric response consisting of a weak surface wind anomaly but a strong vertical circulation extending throughout the troposphere. In the lower troposphere, most of the SST anomaly induced diabatic heating ($\dot{Q}$) is balanced by poleward transient eddy heat and moisture fluxes. Collectively, this response differs from the circulation suggested by linear dynamics, where extratropical SST forcing produces shallow anomalous heating balanced by strong equatorward cold air advection driven by an anomalous, stationary surface low to the east. This latter response, however, is obtained by repeating the same experiment except using a relatively low-resolution (1°, LR) version of CAM5. Comparison to observations suggests that the HR response is closer to nature than the LR response. Strikingly, HR and LR experiments have almost identical vertical profiles of $\dot{Q}$. However, diagnosis of the diabatic quasi-geostrophic ω budget reveals that HR has a substantially stronger $\nabla^2\dot{Q}$ response, which together with upper level mean differential thermal advection balances stronger vertical motion. The results herein suggest that changes in transient eddy heat and moisture fluxes are critical to the overall local atmospheric response to Oyashio front anomalies, which may consequently yield a stronger downstream response. These changes may require high resolution to be fully reproduced, warranting further experiments of this type with other high resolution atmosphere-only and fully coupled GCMs.

1. Introduction

Large-scale extratropical ocean-atmosphere interaction has long been recognized as dominated by atmospheric forcing of the ocean (Davis 1976; Frankignoul and Hasselmann 1977; Frankignoul 1985). However, ocean-atmosphere coupling varies considerably across the mid-latitude ocean basins, with oceanic processes likely to be more important to sea surface temperature (SST) variability in the vicinity of the western boundary currents (WBCs) and their associated SST fronts (Qiu 2000; Nonaka and Xie, 2003; Small et al. 2008; Minobe et al. 2010; Kwon et al. 2010). In the North Pacific, low-frequency WBC anomalies are primarily forced by previous basin-scale wind stress fluctuations via oceanic Rossby wave propagation (Frankignoul et al. 1997; Deser et al. 1999; Qiu 2000; Schneider and Miller 2001). Smirnov et al. (2014) estimated that 40-60% of SST variability in the Kuroshio-Oyashio Extension (KOE) region is driven by oceanic processes, whereas outside of the KOE most SST variability is atmosphere-driven. A key outstanding question is the extent to which these ocean-driven SST anomalies impact the atmosphere, beyond basic thermodynamic air-sea coupling via turbulent boundary layer heat flux exchange that operates throughout the extratropics (Barsugli and Battisti 1998; Frankignoul et al. 1998; Lee et al. 2008). The answer to this question is key to the relevance of large-scale extratropical coupled air-sea modes and could have repercussions on predictability, especially on decadal timescales (Schneider and Miller 2001; Qiu et al. 2014).

Major storm tracks are organized along or just downstream of the main oceanic frontal zones (Nakamura et al. 2004), suggesting that SST variations near the fronts may affect storm track activity and the westerly jets. Some recent modeling and observational

68 evidence supports the view that extratropical SST fronts affect the *climatological*
69 atmospheric state and its variability in the North Pacific (Xu et al. 2011; Sasaki et al.
70 2012), the North Atlantic (Minobe et al. 2008; Minobe et al. 2010), Southern Ocean
71 (Nonaka et al. 2009; Small et al. 2013) and idealized aquaplanet experiments (Brayshaw
72 et al. 2008; Nakamura et al 2008), although how this impact compares to other
73 topographic effects including land-sea contrasts remains unclear (e.g., Saulière et al.
74 2012; Kaspi and Schneider 2013). Furthermore, a better depiction of an SST front
75 improved the numerical simulation of observed cyclones in several studies (Jacobs et al.
76 2008; Booth et al. 2012). One approach to investigating the importance of SST fronts is
77 to compare the mean climates of a model run with or without a SST front. However, by
78 design, the smoothing functions of such "front/no-front" experiments result in SST
79 anomalies with very large amplitude (exceeding 4°C, cf. Fig 2 in Small et al. 2013),
80 spatial extent (e.g., SST anomalies that circumnavigate the earth in aquaplanet
81 experiments) or both, which are never realized in observations.

82 In this paper, we are interested in how realistic changes in the Oyashio Extension
83 front, which is stronger than the Kuroshio Extension front at the sea surface (Nonaka et
84 al. 2006; Frankignoul et al. 2011, hereafter FSKA11; Taguchi et al. 2012), affect the
85 atmosphere during boreal winter, when ocean-atmosphere heat exchange is most
86 vigorous. There is growing evidence that KOE frontal shifts, or alternatively SST
87 anomalies in the KOE region, have a significant influence on the large-scale atmospheric
88 circulation in the Northern Hemisphere (Liu et al. 2006; Frankignoul and Sennéchael
89 2007; Qiu et al. 2007; Okajima et al. 2014). Using a lag of two to six months, FSKA11
90 found that the Oyashio Extension SST frontal shift tends to lead an atmospheric pattern

resembling the North Pacific Oscillation – a meridional dipole with centers near the date line at approximately 35°N and 60°N. However, the use of monthly averaged data and a short record (1982-2008) resulted in a marginal signal to noise ratio, and showed some sensitivity to seasonality. An even stronger sensitivity to seasonality, both in observations and in a coupled model, was shown by Taguchi et al. (2012) who found a high over the Gulf of Alaska and northward shift in the storm track in response to positive KOE SST anomalies in January, but not in February. Gan and Wu (2013) observed a *weakening* of the storm track when the KOE is anomalously warm during early but not late winter. O'Reilly and Czaja (2014) found that when the Kuroshio Extension exhibits a stronger SST front, the atmospheric heat transport by transient eddies is increased in the west Pacific and decreased in the east.

Theoretical and simple modeling studies of the extratropics (Hoskins and Karoly 1981; Hendon and Hartmann 1982; Hall et al. 2001) have shown that the large-scale steady linear atmospheric response to an extratropical SST anomaly, as represented by a low-level diabatic heating anomaly, is a slightly downstream surface cyclonic anomaly. Due to time-mean meridional temperature gradients in the mid-latitudes, this circulation balances the SST induced warming with cold air advection. This results in subsidence (excluding boundary layer Ekman pumping) over the SST anomaly, as column shrinking is required to conserve vorticity and balance the equatorward flow, yielding a baroclinic structure with a downstream upper level high. This basic picture does not tend to support a prominent large-scale atmospheric response to extratropical SST forcing, in contrast to tropical SST forcing of deep anomalous heating, which is balanced by vertical motion

whose corresponding upper level vorticity forcing yields a more pronounced downstream Rossby wave response (Hoskins and Karoly 1981; Sardeshmukh and Hoskins 1988).

The consensus view of the atmospheric response to extratropical SST anomalies (e.g., Kushnir et al. 2002) has been that nonlinear dynamics are essential for the atmospheric response to be significant; specifically, that transient eddy vorticity fluxes must act both to amplify the downstream response and modify it to be equivalent barotropic (Ting 1991; Peng et al. 1997; Hall et al. 2001; Peng and Robinson 2001; Watanabe et al. 2006). Unfortunately, these studies have otherwise yielded inconsistent results, so that their interpretation is complicated by sensitivity to many other factors. For example, a pronounced dependence on seasonality is common, possibly as a consequence of the sensitivity of the downstream response to transient eddy feedbacks (Kushnir et al. 2002). Another issue with past fixed SST experiments is that to get a meaningful response, unrealistically strong SST anomalies have often been prescribed (e.g., Peng et al. 1997; Inatsu et al. 2003; Liu and Wu 2004; see also studies discussed by Kushnir et al. 2002). This implies that realistic SST anomalies would have caused a weak response, although such an approach has been rationalized by suggesting that insufficient model resolution has led to the systematic underestimation of the eddy processes and their amplifying effect. Peng et al. (1997) suggested that relatively higher resolution general circulation models (GCMs) tended to give more consistent results in showing an anomalous equivalent barotropic ridge downstream of positive SST anomalies (broadly consistent with observations). However, at that time, even "higher" resolution models had 2°+ (~250 km) resolution. More recently, Jung et al. (2012) showed that reducing horizontal grid size from 126 km to 39 km in a global climate model produces large

136 improvement in its seasonal forecast skill, with much smaller additional improvement
137 when grid size is further decreased to 16 km and even 10 km. Similar results are found
138 for climate and regional model representation of extratropical cyclone intensity (e.g.,
139 Catto et al. 2010; Willison et al. 2013). Also, higher resolution regional models appear to
140 better represent the impacts of SST fronts on the atmosphere (e.g., Doyle and Warner
141 1993; Taguchi et al. 2009; Woolings et al. 2010; Brachet et al. 2012).

142 This study attempts to address the following: (i) is a state-of-the-art GCM able to
143 produce a robust atmospheric response to a realistic shift in the Oyashio SST front? (ii)
144 Does this response depend on the horizontal resolution of the GCM? And (iii) what
145 physical mechanism(s) governs the local atmospheric response? We investigate the first
146 question by prescribing a SST anomaly that corresponds to an observed shift of the
147 Oyashio Extension front, in the KOE region only, as forcing in a global atmospheric
148 GCM; the impact of resolution is then addressed by running identical experimental
149 ensembles with either a 1° (~90 km) or 0.25° (~23 km) grid. Our main finding is that
150 higher atmospheric model resolution in our experiment yields a strong remote
151 atmospheric response to anomalous surface heating from the Oyashio SST frontal shift,
152 not so much because *remote* feedbacks are altered as because key aspects of the *local*
153 response over the west Pacific are extremely sensitive to model resolution. Thus, in this
154 paper we focus exclusively on diagnosis of the local response, deferring the diagnosis of
155 the remote response to a companion paper.

156 The manuscript is structured as follows. In section 2, we describe the model
157 experimental design, including how the SST forcing boundary condition is developed and
158 prescribed in the National Center for Atmospheric Research Community Atmosphere

159 Model, version 5 (CAM5) GCM, and discuss how we determine observational
160 comparisons to the model results. In section 3, the results of the Oyashio Extension
161 frontal shift experiments using CAM5 at high (0.25°) and relatively low (1°) resolutions
162 are presented. In section 4, we investigate the physical mechanism associated with the
163 atmospheric response. A comparison with observations is presented in section 5. Finally,
164 in section 6, we summarize our findings, highlight outstanding questions, and provide
165 motivation to study the remote response.

166 **2. Experimental Design**

167 *a. Specification of an appropriate Oyashio Extension frontal shift SST anomaly*

168 The Oyashio Extension Index (OEI), developed by FSKA11, is based on the
169 leading empirical orthogonal function of the latitude of the maximum monthly averaged
170 meridional SST gradient (hereafter SST_Y) within the domain 145°-170°E, 35°-47°N. A
171 regression of monthly averaged SST anomalies on the OEI during the extended winter
172 period (November-March) from 1982-2008 is shown in Fig 1a. Hereafter, the polarity in
173 Fig. 1a, which is associated with a *northward* shift in the SST front, is termed the "warm"
174 phase.

175 We are interested in the influence of this frontal shift on the large-scale
176 atmospheric circulation, so here we force an AGCM with a prescribed SST anomaly
177 corresponding to the frontal shift. The risk in this approach is that a substantial portion of
178 the basin-wide SST anomaly (Fig. 1a) may reflect the SST response to atmospheric
179 changes forced by or contemporaneous with the Oyashio Extension shift, which should
180 not be included in a prescribed SST experiment (Barsugli and Battisti 1998; Bretherton
181 and Battisti 2000). That is, we wish to prescribe an SST anomaly that represents only

oceanic forcing of the atmosphere. To focus on the direct frontal influence, we have applied the following to the anomaly in Fig. 1a. Starting with the 140°E meridian and progressing eastward, a 61-point (15.25° span of latitude) tapered cosine window (taper ratio is 0.5) is applied in the meridional direction by centering it on the latitude where the Nov-Mar mean $|SST_Y|$ is maximized *and* only if $|SST_Y| > 1.5°C\ (100\ km)^{-1}$ (anomalies outside of the filter are set to zero). Next, because the fine-scale structure in Fig. 1a may be an artifact of the short data record, a five-point running mean filter is applied 20 times in the *zonal* direction only (to prevent excessive smoothing of the SST front), and then the resultant pattern is scaled by 3 to represent a 3σ shift of the OEI index. The final SST anomaly pattern, shown in Fig. 1b, has SST anomalies with a maximum amplitude of ~1.5K but is limited to 140°-170°E. This region is where Smirnov et al. (2014; cf. their Fig. 5a) found a significant fraction of the SST variability was forced by the ocean, presumably reflecting anomalous heat transport via oceanic advection or eddy activity. A binned scatterplot of point-by-point SST_Y across the Oyashio Extension front over the domain marked by the box in Fig. 1b is shown in Fig. 1c. The OEI captures the northward shifted SST front (~3-4° farther north in the warm phase compared to the cold phase), and suggests that the front is significantly broader in meridional extent during the warm phase. However, note that the *maximum* SST front strength is essentially unchanged (~3.6°C 100 km^{-1}) between the warm and cold phases.

We determine how significant these modifications of the original OEI pattern are by projecting the spatial structure shown in Fig. 1b onto observations to create a "projected OEI" (POEI) time series. The sensitivity of this index to different time periods and resolution is then assessed by comparing three versions constructed using (1)

monthly- and (2) daily-averaged 0.25° NOAA-OI (Reynolds et al. 2007) SST anomalies from 1982-2012, and (3) monthly-averaged 1° OAFlux (Yu and Weller 2007) SST anomalies from 1958-2012. All resulting time series, termed POEI1, 2, and 3, respectively, are standardized to unit variance. During the overlapping period (1982-2012), the two monthly-averaged POEIs based on different datasets (1 and 3) have a 0.98 correlation. The correlation between the original OEI and POEI1 is only 0.56, but the indices are more strongly related (correlation of 0.77) when both are smoothed with a 13-month running mean, suggesting that while there may be non-negligible differences between the two indices on monthly to seasonal time scales they have greater agreement on longer time scales. Moreover, the POEI3, shown in Fig. 2, has a much longer decorrelation time (7 months) compared to the OEI (3 months) so that it may represent the most persistent portion of the OEI SST anomaly and thus be more appropriate for a prescribed SST anomaly experiment. Additionally, while Fig. 1b corresponds to a 3σ departure of the OEI, it amounts to a 1.25σ departure of the POEI3. The correlation between the POEI1 (interpolated to daily values) and daily POEI2 is 0.90, implying that in the daily index sub-monthly variability does not obscure the longer time scales. For reasons discussed in section 5, we use the daily POEI2 (hereafter, just POEI) as the basis for the observational comparison to the GCM simulations.

b. Model details & experimental design

The CAM5 GCM (Neale et al. 2010), coupled to the Community Land Model version 2 and forced by prescribed SST and sea-ice, is used for all experiments in this study. CAM5 is integrated with a finite-volume dynamical core and contains 30 unequally spaced vertical levels using a hybrid pressure-sigma coordinate system.

Notably, there are approximately 8 levels within the boundary layer (> 800 hPa). We run two configurations of the model: a "high-resolution" (HR) version with 0.25° horizontal resolution and time step of 15 min, and a (relatively) "low-resolution" (LR) version with 1° horizontal resolution and time step of 30 min. All parameterization schemes are the same between the HR and LR. Aside from the impacts of linearly interpolating the HR initial and boundary data to the LR grid (slight differences in regions of large topography), all other facets of the two models are identical.

For both configurations, a 25-member ensemble of control simulations is created in the following manner. Using 1 Nov initial atmospheric conditions of 25 different years taken from a previous 0.25° CAM5 simulation (Wehner et al. 2014), we run the CAM5 from 1 Nov through 31 Mar forced by the climatological, monthly-averaged annual cycle of SST derived from the 1982-2011 0.25° NOAA-OI dataset. The same initial land and sea-ice condition are used for all ensemble members. Next, two additional sets of ensembles are conducted in very similar fashion as the control except with the addition ("warm") or subtraction ("cold") of the SST anomaly pattern shown in Fig 1b. The SST anomaly is constant and does not evolve with the annual cycle, which can be justified by the relatively long 7-month decorrelation timescale of the monthly POEI.

3. Atmospheric response to an Oyashio Extension frontal shift

Since we are interested in the equilibrium winter mean response to the Oyashio Extension shift, it is essential to determine (and discard) the time required for model spin-up. Figure 3 shows that the transient atmospheric response to the northward shift of the Oyashio Extension SST front, as depicted by the spatial correlation and spatial root mean square to the equilibrium (Dec-Mar mean) across-front divergence, takes about 15 days

to reach quasi-equilibrium in the HR simulation (in LR, this takes ~20 days, not shown). A similar spin-up time is seen when analyzing the surface heat flux (16 days) and the 2-6 day bandpass 850 hPa $v'T'$ (18 days; not shown). Importantly, in HR the response is similar from month-to-month and is nearly linear when comparing the warm-control and control-cold difference separately (not shown). Thus, hereafter we only discuss the mean December-March atmospheric response, determined from the mean difference between the warm and cold ensembles. Significance is assessed via the Student's t-test assuming that the ensemble members are independent from each other. Finally, since the SST anomaly (warm-cold) in the model simulations represents a +/-1.25σ POEI difference, the results displayed below have been rescaled to represent a 1σ change in the POEI.

The model responses of the HR (left column) and LR (right column) simulations to the prescribed SST anomalies are shown in Fig. 4. The top panels show the net turbulent heat flux (THF; positive upward) and 950 hPa wind responses for HR (Fig. 4a) and LR (Fig. 4b). Both simulations generate a surface cyclone downstream of the SST anomaly, consistent with the expected response to a shallow extratropical heat source (Hoskins and Karoly 1981; Hendon and Hartmann 1982; Peng et al. 1997; Hall et al. 2001; Deser et al. 2007; Smirnov and Vimont 2012). However, the sea-level pressure (SLP) and near-surface wind responses are three to four times stronger in the LR than in the HR simulation. Furthermore, the LR surface anomalies are part of an equivalent barotropic response throughout the entire atmospheric column (not shown but similar to Pitcher et al. 1988 and Kushnir and Lau 1992), though it is only statistically significant from the surface through ~600 hPa. Whereas, there is no significant *local* height response in HR west of the dateline. Surprisingly, the THF response in LR is 15-20 % *greater* than

in HR. This is consistent with much stronger cold and dry air advection over the warm SST anomaly induced by the stronger LR winds compared to the HR. Consequently, while the surface heat fluxes in both the LR and HR act to damp the SST anomaly, the damping is stronger in LR. Based on the surface fluxes alone, the SST anomaly would have an e-folding time-scale of 5 (4) months in the HR (LR) simulations.

While the LR shows a stronger response in the local *horizontal* circulation, the HR shows a substantially stronger response in the *vertical* circulation. Figure 4c,d shows the response of the across-front zonally averaged (145°-165°E, see box in Fig. 1b) circulation [v, ω] and equivalent potential temperature, θ_E. Both HR (Fig. 4c) and LR (Fig. 4d) show upward motion over the positive SST anomalies, consistent with past studies (Feliks et al. 2004; Brachet et al. 2012), but this upward motion in HR extends to the tropopause whereas it is limited to the lower troposphere in LR. In the upper troposphere the circulation forms two cells with northward (southward) flow north (south) of the front in HR, whereas the flow is southward at all latitudes in LR. The larger low-level θ_E anomaly in HR over the warm SST, reflecting both warmer temperatures and enhanced low-level moisture, also reduces the low-level stability (not shown), in a region that is frequently convectively unstable (Czaja and Blunt 2011; Sheldon and Czaja 2014). The zonal wind response is weak in both simulations (not shown): in the LR, zonal wind changes are less than about 1.5 m s^{-1} and are consistent with the cyclonic circulation to the east, while the HR zonal wind changes are of opposite sign and even smaller.

In the western North Pacific, synoptic variability plays a dominant role in transporting heat and moisture (Nakamura et al. 2004; Newman et al. 2012; Kwon and

297 Joyce 2013). Comparing the control climates of HR and LR (contours in Fig. 4e,f) with
298 observations (see section 5) shows HR underestimates 850 hPa transient eddy meridional
299 θ_E flux $\overline{v'\theta_E'}$ (which is functionally equivalent to moist static energy flux) in its core near
300 40°N by only about 8% (54 K m s^{-1} in HR, 59 K m s^{-1} in ERAI) while LR (46 K m s^{-1})
301 underestimates it by 22%. Unfortunately, daily humidity fields were not saved from the
302 model output, so instead this eddy term was determined from monthly averaged
303 covariance as $\overline{v'\theta_E'} = \overline{v\theta_E} - \bar{v}\overline{\theta_E}$, which includes all sub-monthly variability and
304 accounts for a majority of the total climatological 850 hPa $\overline{v'\theta_E'}$ east of Japan (not
305 shown). Aside from the stronger mean $\overline{v'\theta_E'}$ in the storm track core, comparison of the
306 HR and LR mean states does not yield any other major differences.
307 Both the HR and LR exhibit a northward shift of the $\overline{v'\theta_E'}$ with a reduction south
308 of the SST anomaly (Fig. 4e,f), but the increase north of the SST anomaly is more than
309 three times stronger in the HR experiment. The total $\overline{v'\theta_E'}$ response consists of roughly
310 equal contributions from heat and moisture fluxes (not shown). Most of the heat flux
311 response arises from the 2-6 day bandpass filtered, or synoptic, time scales as shown in
312 Figure 5 for the thermal-only component $\overline{v'T'}$ in HR (as noted above, the bandpass
313 moisture flux cannot be determined explicitly). In LR the response is relatively shallow,
314 confined mostly below about 750 hPa, whereas in the HR run the response is much
315 deeper, extending well above 500 hPa, as shown in the across-front vertical cross sections
316 of $\overline{v'\theta_E'}$ (Fig. 6a,b). Equally striking differences are seen in sub-monthly $\overline{v'^2}$ (Fig. 6c,d),
317 which increases north of the front in HR but decreases south of the front in LR. The
318 broadening of the storm track at upper levels in HR is notable and consistent with a
319 broader SST front (Fig. 1c) but does not reach the 95% significance level. Note that the

upper-level $\overline{v'^2}$ is about 20% stronger in the HR control compared to the LR control (black contours in Fig. 6c,d), though even HR still slightly underestimates $\overline{v'^2}$ in ERAI (not shown).

Collectively, the HR simulation places a much greater emphasis on eddy transport in a region where fluxes of heat and moisture occur predominantly with the passage of warm and cold fronts (James 1992). To gauge how the HR and LR treat such passages and their sensitivity to the SST anomaly, Fig. 7 shows a composite of anomalous SLP (contour) and 2-8 day band-pass filtered 850 hPa $v'T'$ (color) when an atmospheric front appears in the black box shown in panels a-d (we use $v'T'$ instead of $v'\theta_E'$ because daily q was not archived). Fronts are identified in both the warm and cold simulations of HR and LR when the thermal front parameter (TFP), a scalar value based on the gradient of the magnitude of 6-hourly averaged 850 hPa potential temperature (see Table 1 in Hewson 1998). Using a TFP exceedance threshold value of 0.15 K per 100 km^2 (Renard and Clarke 1965; Booth et al. 2012), a front is identified in the box in Fig. 7 about 1 out of every 6 days. To avoid very localized, potentially misleading features, this criterion must be met at two or more neighboring grid points. Figure 7a-d shows that the composite SLP field is characterized by a 6-7 hPa cyclonic anomaly within the box with a 5-6 hPa anticyclonic anomaly ~20° east for both the warm and cold simulations of HR and LR, with $v'T'$ consistent with northward advection of warm air in a midlatitude cyclone's warm sector. For fronts passing through this box, $v'T'$ is about 10% stronger in the HR than LR simulations for both warm and cold phases (cf. Figs. 7a vs. 7b and 7c vs. 7d), even though the SLP composites are nearly identical, similar to the difference between the HR and LR control runs (the black contours in Fig. 4e,f). However, for the

343 warm minus cold response (Fig. 7e,f), the SST anomaly has a much greater impact on
344 heat flux associated with frontal passage in the HR, with a dipole in the $v'T'$ response
345 roughly straddling the SST front, while the LR only captures the (weaker) southern
346 portion of the response.

347 Both models have enhanced cloud formation and precipitation resulting from the
348 warm SST anomaly though the response is shifted slightly poleward (and consistent with
349 a more robust storm track shift) in HR compared to LR (Fig. 8). However, while the
350 magnitude of the precipitation response is similar in HR and LR (Fig. 8a,b), the
351 precipitable water response in HR is more than twice as large. There is also a
352 corresponding increase in the cloud water content in the HR simulation (not shown). The
353 much higher levels of PW and cloud water are consistent with the increased transient
354 eddy moisture flux convergence in the HR simulation (not shown, but the differences are
355 similar to Fig. 4e,f) as well as the stronger advection of dry air from the northeast and a
356 weakening of the background westerlies in the LR simulation (Fig. 4a,b). That is, even
357 though the precipitation response over the SST anomaly is similar, in LR there is a local
358 balance between increased evaporation and precipitation, while in HR, storms converge
359 moisture into the storm track/jet stream that can subsequently be transported downstream
360 (not shown but see Fig. 15a,b).

361 Figure 9 shows the stark difference in the SLP and precipitation response from the
362 standpoint of an individual synoptic storm. This event is chosen from the 4th day of the
363 model runs (November 4th) where a particular weather feature could still be identified in
364 all four simulations (warm/cold, HR/LR). One caveat is that this may not portray the
365 sensitivity of the *equilibrium* response as Fig. 3 showed this requires roughly 2 weeks.

Nonetheless, Fig. 9 shows that HR depicts a slightly stronger cyclone than LR, located near 40°N, 160°E. HR contains two frontal-like precipitation bands, while the LR shows one main band in the immediate vicinity of the cyclone center. However, the largest differences appear by taking the warm – cold response. Figure 9e,f shows that the precipitation response in HR is roughly four times stronger and more coherent than LR, though both models depict a northward shift in precipitation to first order. Additionally, the HR shows a substantially stronger response in SLP, with a 2-3 hPa dipole straddling the cyclone center. Meanwhile, the LR shows a broader cyclonic anomaly that is located much farther west. Figure 9 is not meant to be a generalization across all synoptic disturbances, but instead shows the surprising sensitivity to atmospheric resolution at the frontal scale.

4. Diagnosis of physical mechanisms

In response to the poleward shift of the SST front, the HR and LR simulations each, to different extents, develop a near-surface cyclonic circulation to the east of the warm SST anomaly, with enhanced θ_E, upward motion and transient eddy heat flux divergence above the SST anomaly. However, the relative importance of these processes is very different, such that while the LR primarily balances the warm SST by a mean circulation change advecting cold and dry air southwards, the HR primarily balances the enhanced heat and moisture through transient eddies transporting heat and moisture northwards, probably via frontal passages. In this section, we further quantify these key differences by constructing budgets using the thermodynamic and ω equations.

387 *a. Thermodynamic budget*

388 First, we diagnose how heat is exchanged at the air-sea interface and within the
389 atmospheric column. The processes that balance the diabatic heating $\dot{Q}$ resulting from
390 the SST anomalies are determined from the time-mean thermodynamic equation, written
391 as:

$$\underbrace{\bar{u}\frac{\partial \bar{T}}{\partial x}}_{\text{I}} + \underbrace{\frac{\partial}{\partial x}\overline{u'T'}}_{\text{II}} + \underbrace{\bar{v}\frac{\partial \bar{T}}{\partial y}}_{\text{III}} + \underbrace{\frac{\partial}{\partial y}\overline{v'T'}}_{\text{IV}} + \underbrace{\left[\bar{\omega}\frac{\partial \bar{T}}{\partial p} - \frac{\kappa}{p}\bar{\omega}\bar{T}\right]}_{\text{V}} + \underbrace{\left[\overline{\omega'\frac{\partial T'}{\partial p}} - \frac{\kappa}{p}\overline{\omega'T'}\right]}_{\text{VI}} = \underbrace{\bar{\dot{Q}}}_{\text{VII}} \quad (1)$$

392

393 where overbars represent the ensemble climatological mean for each month, primes
394 represent departures from that mean, $\kappa = R / C_P$, where R is 287 J kg^{-1} K^{-1} and C_P is 1004
395 J kg^{-1} K^{-1} and all other terms assume their typical meteorological conventions. The HR
396 data are linearly interpolated to the LR grid and the budget is calculated for each month,
397 separately, and then averaged to form a Dec-Mar mean. Term VII is from direct model
398 output and the budget is nearly closed with the residual being a few percent of the sum
399 from the remaining terms, except in very close proximity to orography. The warm and
400 cold ensembles each have their own climatological means, and we calculate each term
401 separately for the warm and cold ensembles of both HR and LR. The mean difference
402 between the warm and cold ensembles is termed the response to the SST frontal shift.
403 Figure 10 shows the net response of the horizontal (terms I-IV), vertical (terms
404 V,VI) and $\bar{\dot{Q}}$ components of (1) separately. In the lowest levels (1000-800 hPa), ω is
405 necessarily small, leaving the horizontal terms [I-IV in (1)] to balance $\bar{\dot{Q}}$. Consistent with
406 the stronger THF in Fig. 4b, $\bar{\dot{Q}}$ is about 15% stronger in LR than in the HR (cf. Figs. 10e

and f), and therefore cooling from horizontal heat transport is also stronger. Above this layer, where $\bar{\dot{Q}}$ becomes slightly stronger in HR than LR, the most notable difference between the two simulations is that cooling by the vertical transport terms [V-VI in (1)] is 80% stronger in HR. Indeed, vertical transport is so strong and vertically extensive in HR that above 500 hPa it must be balanced by warming from the horizontal transport terms (Fig. 10a). Little to no such net response is seen at upper levels in LR.

To differentiate between the relative importance of eddy heat flux divergence and mean thermal advection, in Fig. 11 we next show each of the seven terms in (1) averaged within the region 145º-165ºE, 35°-43°N (i.e. over the positive SST anomaly; see dotted lines in Fig. 10). Near the surface the meridional heat transport terms largely balance $\bar{\dot{Q}}$, but for the LR the mean transport dominates the eddy transport whereas for the HR the eddy transport is about 60 % larger than the mean transport (Fig. 11c) and has much greater vertical extent. Recall that the total (i.e. sub-monthly) eddy response is dominated by the 2-6 day synoptic timescales (Fig. 5). In the middle and upper troposphere, the large difference in the vertical transport between HR and LR is due to the mean ω circulation (Fig. 11d). For the LR in this region, mean zonal and meridional terms are large but mostly offset (cf. Figs 11b and 11c), whereas the primary HR balance is between the combined mean horizontal and vertical transports. Overall, the thermodynamic budget confirms that horizontal eddy transports (lower troposphere) and strong vertical motion (mid troposphere) are much more important for balancing $\bar{\dot{Q}}$ in HR than in LR simulations.

428 *b. Omega equation*

429 The stronger ω response in HR seen in Fig. 4c,d raises the question of what
430 physical mechanism(s) correspond to this difference. To investigate, we calculate
431 contributions to ω using a modified quasi-geostrophic (QG) form of the generalized ω
432 equation that includes diabatic effects (Krishnamurti 1968; Trenberth 1978; Raisanen
433 1995). Unlike past studies such as Pauley and Nieman (1992) and Raisanen (1995), we
434 focus on the mean ω as opposed to an individual synoptic event. The modified QG-ω
435 equation can be written as:

$$\left[\bar{\sigma}\nabla^2 + f^2\frac{\partial^2}{\partial p^2}\right]\bar{\omega} =$$

$$\nabla^2\left[\bar{V}_g\cdot\nabla\left(-\frac{\partial\bar{\phi}}{\partial p}\right) + \overline{V'_g\cdot\nabla\left(-\frac{\partial\phi'}{\partial p}\right)}\right] + f\frac{\partial}{\partial p}\left[\bar{V}_g\cdot\nabla\left(\bar{\zeta}_g + f\right) + \overline{V'_g\cdot\nabla\zeta'_g}\right] - \frac{\kappa}{p}\nabla^2\bar{\dot{Q}} \qquad (2)$$

I II III IV V

436

437 where σ is the wintertime spatially varying Dec-Mar mean static stability
438 $\sigma(x,y,p) = -\dfrac{RT}{p\theta}\dfrac{\partial\theta}{\partial p}$, ϕ is the geopotential height. Terms I and II are the mean and eddy
439 components of the differential thermal advection, while terms III and IV are the mean
440 and eddy components of the differential vorticity advection. Generally, thermal
441 (vorticity) advection is more important in the lower (mid and upper) troposphere;
442 however, there is often strong cancellation between the two (Hoskins et al. 1978;
443 Billingsley 1998) and investigating each term separately may be beneficial.

444 The recalculated ω response (hereafter ω^R) is accomplished via successive
445 relaxation by forcing with the sum of the r.h.s. of (2). Details of the calculation are in
446 Appendix A. Figure 12a,b shows the across-front response in ω compared with ω^R for

447 HR and LR. There are regions where ω^R differs from ω, but generally this difference is
448 less than 20%. Over the warm SST (36°-42°N), ω^R overestimates the upward motion, but
449 except near the tropopause this discrepancy is relatively small. Given this, the ω^R
450 response can be used as a proxy for ω and Fig. 12c-f shows the dominant terms in (2);
451 terms II (eddy thermal), III (mean vorticity) and IV (eddy vorticity) are small (less than
452 one contour) and thus not shown. Over the SST anomaly in the lower to mid troposphere
453 (from the surface to 500 hPa), the HR simulation generates vertical motion that is about
454 40% stronger than LR and is balanced by a stronger diabatic term V. This might appear
455 to contradict the earlier observation that the low level LR heating is actually stronger than
456 HR (cf. Fig. 10e and f), but it is the finer scale structure of $\overline{\dot{Q}}$ as measured by $\overline{\nabla^2\dot{Q}}$ (see
457 dashed contours of Fig. 10e,f) that is commensurately stronger in HR at lower levels.
458 That is, the narrowness of the diabatic heating balances the stronger ω field, though
459 causality cannot be determined via the diagnostic equation (2).
460 The other major difference between ω^R in the two simulations is mainly in the
461 mid- and upper-troposphere where mean differential thermal advection [term (I) in (2);
462 Fig 12c,d] generates stronger upward motion in the HR simulation. Since this region has
463 a significant mean meridional temperature gradient and weak poleward flow (not shown),
464 enhanced upward motion could be maintained by a shift in the temperature gradient
465 and/or by changes in the circulation. To determine which is more important, we
466 recalculate ω^R but using several modified forms of term I, as shown in Fig. 13. First, Fig.
467 13b shows that when u and v are both set to be their control climatological values, the ω^R
468 response is much weaker and nearly of opposite sign as the full term I forcing (cf. Fig.
469 13a), implying that changes in the mean T field are an insignificant contributor to term I.

Next, when T is set to climatology (Fig. 13c), the ω^R is nearly identical to full forcing, confirming that the anomalous wind is responsible for balancing the upper-level ω^R. Lastly, when T and u are set to climatology (Fig. 13d), the resulting ω^R is almost identical to the full forcing, showing that it is specifically the anomalous v that contributes most strongly to balancing the upper-level ω^R in HR. The impact of anomalous u is not negligible and has about 20% of the impact of v, but is shifted further south than the main region of upward motion seen in Fig. 13a.

5. **Observational comparison**

Properly diagnosing extratropical air-sea interactions in observations is challenging. Simultaneous atmosphere-ocean statistics can be misleading due to the coupled nature of the problem and the differing oceanic and atmospheric dynamical time scales (Frankignoul and Hasselmann 1977). To address this issue, empirical analysis in the extratropics must include some temporal lag that is longer than the intrinsic atmospheric persistence of a few days to weeks (Frankignoul and Kestenare 2002) or, ideally, empirically estimate coupled air-sea dynamics explicitly (Smirnov et al. 2014). This is difficult in short datasets of a multivariate system in which slowly evolving oceanic forcing may produce atmospheric responses co-existing with faster coupled air-sea variability, as well as oceanic variability forced primarily by the atmosphere, with corresponding spatial patterns that are neither identical nor orthogonal.

As noted in the introduction, past observational analyses on the impact of the Oyashio SST front find pronounced signals but do not uniformly agree, especially concerning the remote atmospheric response. We do not aim to solve that problem in this paper. However, given the strong sensitivity of the results to model resolution, it is

493 natural to ask whether the local atmospheric response of either experiment is consistent
494 with nature. We do not expect an identical match of course, since although the SST
495 anomaly used in our experiment has realistic amplitude and pattern it was held fixed and
496 specified only within the POEI region. Still, to create an observational comparison to
497 section 3 we have regressed various atmospheric variables on the POEI for lags ranging
498 from several days to 2 months, with the POEI both leading and lagging the atmosphere,
499 roughly similar to the FSKA11 approach. We have also examined both daily and monthly
500 averaged data. Choosing one representative lag and data sampling interval is difficult as
501 no single lag time captures the response of all variables, possibly because (i) there is a
502 transient atmospheric response to the Oyashio Extension shift that is dependent on lag,
503 and (ii) each atmospheric variable decorrelates on a different timescale. For display
504 purposes, we show a lag regression of daily wintertime (November-March) data when the
505 POEI leads the atmosphere by 14 days, which should be long enough to mainly capture
506 the atmospheric response to the POEI (as most atmospheric variables are nearly fully
507 decorrelated after two weeks), and also seems appropriate based on the earlier discussion
508 of the model response equilibration time (Fig. 3). For comparison, we also show the
509 simultaneous regression between the atmosphere and the POEI, but note that this is
510 difficult to interpret since it can contain both the forcing of and response to the POEI SST
511 anomaly.

512 In general, the regression amplitude depends on lag, sometimes strongly, but the
513 spatial structure is fairly consistent. Using daily data resulted in a 20-40% stronger signal
514 compared to using monthly data, but results are otherwise qualitatively similar (not
515 shown). The ERAI does not have daily values of sensible and latent heat flux, so the 1°

516 Objectively Analyzed air-sea fluxes (OAFlux; Yu and Weller 2007) dataset is used for
517 these variables. Also, since El-Nino Southern Oscillation (ENSO) variability has a strong
518 teleconnection to the North Pacific (e.g. Alexander et al. 2002), we remove the co-
519 variability with ENSO from both the POEI and all atmospheric variables by a linear
520 regression using the daily Nino3.4 index. This generally reduces the amplitude of
521 regression coefficients by up to 15% (mostly east of the dateline) but leaves the spatial
522 structures unchanged.

523 Additionally, FSKA11 suggested that the meridionally confined nature of the
524 Oyashio Extension SST front variability could make it difficult to diagnose the
525 atmospheric response in coarse-resolution datasets. We compared the across-front
526 regression of pressure velocity (ω, negative upward) on the POEI using the 0.7° ERA-
527 Interim (ERAI; Uppala et al. 2008; http://data-portal.ecmwf.int/data/d/interim_daily/)
528 dataset with the 2.5° National Center for Environmental Prediction Reanalysis I (NCEP-
529 R1; Kalnay et al. 1996) over the 1982-2012 period and found a 40% stronger signal in the
530 former (not shown). Here we chose the enhanced ERAI resolution (time range: 1979-
531 present) over the longer data record provided by NCEP-R1 (time range: 1948-present).

532 With the many above caveats in mind, in Fig. 14 we show the same fields as
533 displayed in Fig. 4, but based on regressions of observed data onto the daily POEI at 0-
534 day (left column) and 14-day lags (right column). In the observed regression, positive
535 POEI values are associated with strong THF from the ocean to atmosphere on the
536 southern periphery of the SST front (36°-42°N) roughly at a rate of ~30 W m^{-2} per °C,
537 consistent with previous estimates (Frankignoul and Kestenare 2002; Park et al. 2005).
538 Note that weaker values in Fig. 14a appear to be the result of the contemporaneous state

539 of the POEI and atmosphere, with larger values resulting when the POEI leads THF by
540 14 days (Fig. 14b), consistent with oceanic forcing of the atmosphere (see Fig. 21 in
541 Frankignoul 1985). The 14-day regression (i) has a 40% weaker θ_E signal and (ii) limits
542 the upward vertical motion to the immediate SST anomaly region.

543 In general the observations seem more broadly consistent with the HR than the
544 LR model results. In terms of the response to POEI SST anomalies, the observed
545 regression appears to have a broader area of upward THF than either the HR or LR
546 simulation, which could be due to the limited spatial extent of the prescribed SST
547 anomaly in the model, but the observed and model amplitudes appear comparable. The
548 lack of significant wind anomalies in the observed regression appears more consistent
549 with the HR, suggesting that LR may be overemphasizing the importance of the mean
550 circulation response in balancing anomalous heat from the SST. Additionally, the vertical
551 extent of the upward motion over the SST anomaly in the HR resembles the observed
552 pattern, as does the upper-level outflow that is symmetric or slightly northward, whereas
553 the LR (Fig. 4d) has southward flow at all levels.

554 Finally, both the simultaneous and 14-day lag regression (Figs. 14e,f; note that
555 using lags of 21 and 28 days results in a very similar pattern as the 14-day) indicate a
556 northward shift of $\overline{v'\theta_E'}$, but primarily indicate a much stronger reduction of $\overline{v'\theta_E'}$ south
557 of the SST front, especially Fig. 14f that appears markedly different from Fig. 14e and
558 appears to better match LR. However, we note that the *divergence* of $\overline{v'\theta_E'}$ centered over
559 the warm SST anomaly is the same in both panels, with the location and amplitude better
560 matching the HR results (not shown). Collectively, it appears the observed regressions

561 better match HR due to (i) significantly more active eddy heat transport response and (ii)
562 deeper response in ω.

563 **6. Discussion and conclusion**

564 In a high resolution (0.25º) version of the NCAR CAM5, a meridional shift of the
565 Oyashio Extension SST front is shown to locally force a robust atmospheric response
566 dominated by changes in the eddy heat and moisture transports. However, in the
567 corresponding low resolution (1°) simulations, the local atmospheric response exhibits
568 strong heating by surface fluxes that is balanced by the mean equatorward advection of
569 cold air, consistent with the paradigm of a steady linear response to a near surface heat
570 source (see Hoskins and Karoly 1981). In the higher resolution simulation, we noted a
571 substantially weaker surface circulation (Fig. 4a,b), stronger and deeper vertical motion
572 (Fig. 4c,d), and significantly stronger transient eddy moist static energy flux as key
573 responses to the SST anomaly. Furthermore, it appeared that the latter difference could be
574 seen on average in individual synoptic fronts (Fig. 7,9).

575 A number of previous modeling studies have suggested that heat from an
576 extratropical SST anomaly is transferred into the lower troposphere where it directly
577 forces the atmospheric response, with transient eddy flux feedbacks primarily important
578 for modifying the *downstream* upper level circulation anomaly (Peng et al. 2003; Peng
579 and Whitaker 1999; Hall et al. 2001; Yulaeva et al. 2001; Kushnir et al. 2002). In
580 contrast, we find that transient eddies impact the *local* heat balance through changes in
581 the transient eddy moist static energy flux. That is, extratropical cyclones respond to the
582 underlying SST anomaly in the Oyashio Extension front region by transporting much of
583 the anomalous heat northward, so that even under linear theory the weaker residual

584 heating could be expected to produce only a weak surface low to the east. As the
585 downstream low and its southward advection of cold, dry air are reduced, subsidence
586 associated with vortex shrinking over the heating region is also reduced.

587 Some issues in our experimental design limit interpretation of our results. First,
588 when comparing HR to LR responses, the impact of better resolving the SST gradient
589 cannot be distinguished from intrinsic differences between the 0.25° and 1° versions of
590 CAM5. This issue could be addressed by re-running the HR experiments but with the 1°
591 SST grid used by LR. Second, because some of the SST anomaly in the central and
592 eastern Pacific related to an Oyashio Extension shift (Fig. 1a) represents coupling to or
593 forcing by the atmosphere (Smirnov et al. 2014), we employed a conservative
594 experimental approach by prescribing a very spatially confined SST anomaly; however,
595 this approach still ignores potential feedbacks due to air-sea coupling. Also, the model
596 SST anomaly is held fixed in time, whereas in observations its decorrelation time scale is
597 7 months and in the HR it would have ~5 month decorrelation time scale if allowed to
598 decay due to surface heat fluxes.

599 While it seems intuitive that the HR better resolves frontal circulations and
600 associated ω, we have not determined why the transient eddy heat and moisture flux
601 *responses* are so sensitive to model resolution. Moist diabatic processes appear to affect
602 how SST fronts could influence extratropical cyclone development (Fig. 9; also Booth et
603 al. 2012; Deremble et al. 2012; Willison et al. 2013), and Willison et al. (2013) found
604 increased moist diabatic creation of potential vorticity during cyclogenesis between two
605 regional model resolutions roughly corresponding to our LR and HR models. Our SST
606 anomaly might be special in shape and/or location, such that different SST anomalies in

607 the HR model would produce less dramatic results, although it seems reasonable to
608 suggest that locating the SST anomaly within the climatological storm track yields a
609 greater impact on the transient eddy heat flux than elsewhere. Moreover, our HR result
610 could be unique to CAM5, so it should be confirmed with other high resolution GCMs.
611 On the other hand, two recent GCM studies have shown SST frontal anomalies to have
612 similarly pronounced impacts on transient eddy heat flux, as well as relatively weaker
613 impacts on meridional eddy wind variance, in the North Pacific (Taguchi et al. 2009) and
614 in the North Atlantic (Small et al. 2013). Still, our HR results (especially Fig. 7 and 9)
615 strongly suggest that better understanding of how SST anomalies affect North Pacific
616 cyclogenesis, including associated heat and moisture transports, and how model
617 resolution impacts the accurate simulation of these processes, is essential to determining
618 the impact of Oyashio Extension frontal shifts in nature.

619 Though the focus of this manuscript is on the local response to the Oyashio
620 Extension shift, it is arguably the remote response that is more relevant to society since
621 variability in the Oyashio Extension frontal region projects onto the larger-scale Pacific
622 decadal oscillation (Mantua et al. 1997; Schneider and Cornuelle 2005; Kwon et al. 2010;
623 Newman 2013; Seo et al. 2014). Given the stronger and deeper local atmospheric
624 response in the HR simulation, with a pronounced divergence anomaly located in the jet
625 core at around 300 hPa, it is not entirely surprising that striking differences between HR
626 and LR also exist across the entire North Pacific basin, which is shown in Fig. 15 for 800
627 hPa θ_E and 300 hPa geopotential height. In HR, the θ_E response is stronger locally and
628 extends eastward across a substantial portion of the North Pacific, culminating with a
629 strong anomalous anticyclone in the Gulf of Alaska and substantially reduced

precipitation along the northwest coast of North American (not shown). Meanwhile, in LR, there is no significant response north of 40°N, but a weak response in the subtropics as the anomalous local cyclonic circulation advects relatively high θ_E air southward and eastward. A full diagnosis of this remote response is underway.

Acknowledgements.

The authors thank Justin Small and Shoshiro Minobe for stimulating discussions, as well as Hisashi Nakamura and two anonymous reviewers for constructive suggestions. Michael Wehner provided the 0.25° initial condition files for CAM5. We also gratefully acknowledge funding provided by NSF to DS and MN [AGS CLD 1035325] and Y-OK and CF [AGS CLD 1035423], and by DOE to Y-OK [DE-SC0007052].

641 Appendix A

642 Details of the modified QG-ω budget

643 Forcing terms I-IV in (2) only require ϕ from which u_g and v_g and ζ_g and their
644 spatial and vertical derivatives are approximated via a centered finite difference scheme.
645 For the extended winter months (Dec-Mar) of the simulations, forcing terms I and III are
646 found by separately averaging over the warm and cold ensembles during that period.
647 Meanwhile, terms II and IV require anomalous values, which are found by removing the
648 monthly ensemble mean separately for the warm and cold ensembles. Data is on 20
649 pressure levels that are log-linearly interpolated from the model hybrid (pressure and
650 sigma) coordinates to pressure levels. Using daily averages reduces the mean thermal and
651 momentum covariance by 20 % compared to four-times daily data, but the calculated ω
652 response is only altered by less than 10 %. Thus, daily average data are used due to a
653 substantial reduction in required computational time. Furthermore, the data is linearly
654 interpolated to the LR ~1°x1° grid. The effect of interpolation is only important in the
655 immediate vicinity of topography and influences ω^R less than 3 % across the ocean grid
656 points (not shown).

657 To generate ω from (2), successive relaxation is used after imposing a zero
658 boundary condition at the top and bottom levels as well as the horizontal boundaries of
659 the domain [the domain is 110°-200°E, 15°-65°N; see Nieman (1990) for further details].
660 With this homogeneous boundary condition, the forcing from each term can be linearly
661 separated. With a relaxation parameter (see Krishnamurti 1968; Nieman 1990) of 0.88,
662 implying "underrelaxation", 400 iterations are sufficient to determine ω. The recalculated
663 ω, hereafter ω^R, is found for the warm and cold ensembles of HR and LR, separately, and

664 then the warm-cold difference is the response. Figure 12a,b shows that ω^R compares well
665 with the model-generated ω, with a residual less than 10 % for LR, and 20 % for HR
666 (except in the in localized regions in the upper-levels; see Fig. 12a,b). The differences
667 could arise from the neglect of friction terms, the use of daily averaged data that would
668 underestimate the impact of the covariance terms, or from interpolation (only for HR as
669 LR is calculated on its native grid). Interestingly, using the full wind (instead of the
670 geostrophic wind) and including the tilting and twisting terms in the ω equation (Pauley
671 and Nieman 1992; Raisanen 1995) had very little impact on ω^R (not shown), suggesting
672 that the modified QG approximation with inclusion of diabatic heating yields a
673 satisfactory approximation. This may not be the case on a storm-by-storm analysis.
674

675 # References

676 Alexander, M. A., et al., 2002: The Atmospheric Bridge: The Influence of ENSO
677 Teleconnections on Air-Sea Interaction over the Global Oceans. *J. Climate*, **15**, 2205-
678 2231.

679 Barsugli, J., and D. Battisti, 1998: The basic effects of atmosphere–ocean thermal
680 coupling on midlatitude variability. *J. Atmos. Sci.*, **55**, 477–493.

681 Billingsley, D., 1998: A review of QG theory – Part III: A different approach. *National*
682 *Weather Digest*, **22**, 3-10.

683 Booth, J.F., L Thompson, J. Patoux and K.A. Kelly, 2012: Sensitivity of Midlatitude
684 Storm Intensification to Perturbations in the Sea Surface Temperature near the Gulf
685 Stream. *Mon. Wea. Rev.*, **140**, 1241-1256.

686 Brayshaw, D. J., B. Hoskins, and M. Blackburn, 2008: The Storm-Track Response to
687 Idealized SST Perturbations in an Aquaplanet GCM. *J. Atmos. Sci.*, **65**, 2842-2860.

688 Brachet, S. and co-authors, 2012: Atmospheric circulations induced by a midlatitude SST
689 front: A GCM study. *J. Climate*, **25**, 1847-1853.

690 Bretherton, C., and D. Battisti, 2000: Interpretation of the results from atmospheric
691 general circulation models forced by the time history of the observed sea surface
692 temperature distribution. *Geophys. Res. Lett.*, **27**, 767–770.

693 Catto, J.L., L.C. Shaffrey, and K.I. Hodges, 2010: Can Climate Models Capture the
694 Structure of Extratropical Cyclones? *J. Climate*, **23**, 1621–1635.

695 Czaja A, and N. Blunt, 2011. A new mechanism for ocean–atmosphere coupling in
696 midlatitudes. *Q. J. R.Meteorol. Soc.* **137**, 1095–1101.

697 Davis, R.E., 1976: Predictability of Sea Surface Temperature and Sea Level Pressure
698 Anomalies over the North Pacific Ocean. *J. Phys. Oceanogr.*, **6**, 249–266.
699 Deremble, B., G. Lapeyre, and M. Ghil, 2012: Atmospheric dynamics triggered by an
700 oceanic SST front in a moist quasigeostrophic model. *J. Atmos. Sci.*, **69**, 1617-1632.
701 Deser, C., M.A. Alexander, and M.S. Timlin, 1999: Evidence for a wind-driven
702 intensification of the Kuroshio Current Extension from the 1970's to the 1980's. *J.*
703 *Climate*, **12**, 1697-1706.
704 Deser, C., R. A. Tomas, and S. Peng, 2007: The Transient Atmospheric Circulation
705 Response to North Atlantic SST and Sea Ice Anomalies. *J. Climate*, **20**, 4751-4767.
706 Doyle, J. D. and T. T. Warner, 1993: The impact of the sea surface temperature
707 resolution on mesoscale coastal processes during GALE IOP 2. *Mon. Wea. Rev.*, 121,
708 313-334.
709 Feliks, Y., M. Ghil, and E. Simonnet, 2004: Low-Frequency Variability in the
710 Midlatitude Atmosphere Induced by an Oceanic Thermal Front. *J. Atmos. Sci.*, **61**, 961-
711 981.
712 Frankignoul, C. and K. Hasselmann, 1977: Stochastic climate models, Part II:
713 Application to sea-surface temperature anomalies and thermocline variability. *Tellus*, **29**,
714 289–305.
715 Frankignoul, C., 1985: Sea Surface Temperature Anomalies, Planetary Waves, and Air-
716 Sea Feedback in the Middle Latitudes. *Rev. Geophys.*, 23, 357-390.
717 Frankignoul, C., P. Muller, and E. Zorita, 1997: A simple model of the decadal response
718 of the ocean to stochastic wind forcing. *J. Phys. Oceanography*, **27**, 1533-1546.

719 Frankignoul, C., A. Czaja, and B. L'Hedever, 1998: Air-sea feedback in the North
720 Atlantic and surface boundary conditions for ocean models. *J. Climate*, **11**, 2310-2324.
721 Frankignoul, C., and E. Kestenare, 2002: The surface heat flux feedback. Part I: estimates
722 from observations in the Atlantic and North Pacific. *Clim. Dyn.*, **19**, 633-647.
723 Frankignoul, C. and N. Sennechael, 2007: Observed influence of North Pacific SST
724 anomalies on the atmospheric circulation. *J. Climate*, **20**, 592-606.
725 Frankignoul, C., N. Sennechael, Y. Kwon, and M. Alexander, 2011: Influence of the
726 meridional shifts of the Kuroshio and the Oyashio Extensions on the atmospheric
727 circulation. *J. Climate*, **24**, 762–777.
728 Gan, B. and L. Wu, 2013: Seasonal and Long-Term Coupling between Wintertime Storm
729 Tracks and Sea Surface Temperature in the North Pacific. *J. Climate*, **26**, 6123–6136.
730 Hall, N. M. J., Derome, J. and H. Lin, 2001: The Extratropical Signal Generated by a
731 Midlatitude SST Anomaly. Part I: Sensitivity at Equilibrium. *J. Climate*, **14**, 2035-2053.
732 Hendon, H.H., and D.L. Hartmann, 1982: Stationary waves on a sphere: Sensitivity to
733 thermal feedback. *J. Atmos. Sci.*, **39**, 1905-1920.
734 Hewson, T. D., 1998: Objective fronts. *Meteor. Appl.*, **5**, 37–65.
735 Hoskins, B.J, I. Draghici, and H.C. Davies, 1978: A new look at the omega equation.
736 *Quart. J. R. Met. Soc.*, **104**, 31-38.
737 Hoskins, B.J., and D. J. Karoly, 1981: The steady linear response of a spherical
738 atmosphere to thermal and orographic forcing. *J. Atmos. Sci.*, **38**, 1179–1196.
739 Inatsu, M., H. Mukokougawa, S.-P. Xie, 2003: Atmospheric response to zonal variations
740 in midlatitude SST: transient and stationary eddies and their feedback. *J. Climate*, **16**,
741 3314-3329.

742 Jacobs, N.A., S. Raman , G. M. Lackmann, and P. P. Childs Jr., 2008: The influence of
743 the Gulf Stream induced SST gradients on the US East Coast winter storm of 24–25
744 January 2000, *International Journal of Remote Sensing*, **29**, 6145-6174.
745 James, Ian N. *Introduction to circulating atmospheres*. Cambridge University Press,
746 1995.
747 Jung, T. and co-authors, 2012: High-resolution global climate simulations with the
748 ECMWF model in Project Athena: Experimental design, model climate and seasonal
749 forecast skill. *J. Climate*, **25**, 3155-3172.
750 Kalnay, E. and co-authors, 1996: The NCEP/NCAR 40-year reanalysis project. *Bull.*
751 *Amer. Meteor. Soc.*, **77**, 437-471.
752 Kaspi, Y., and T. Schneider, 2013: The Role of Stationary Eddies in Shaping Midlatitude
753 Storm Tracks. *J. Atmos. Sci.*, **70**, 2596–2613.
754 Krishnamurti, T.N., 1968: A diagnostic balance model for studies of weather systems of
755 low and high latitudes, Rossby number less than 1. *Mon. Wea. Rev.*, **96**, 197-207.
756 Kushnir, Y., and N.-C. Lau, 1992: The general circulation model response to a North
757 Pacific SST anomaly: Dependence on time scale and pattern polarity. *J. Climate*, **5**, 271-
758 283.
759 Kushnir, Y., W. Robinson, I. Blade, N. Hall, S. Peng, and R. Sutton, 2002: Atmospheric
760 GCM response to extratropical SST anomalies: Synthesis and evaluation. *J. Climate*, **15**,
761 2233–2256.
762 Kwon, Y., M. Alexander, N. Bond, C. Frankignoul, H. Nakamura, B. Qiu, and L.
763 Thompson, 2010: Role of the Gulf Stream and Kuroshio–Oyashio systems in large-scale
764 atmosphere–ocean interaction: A review. *J. Climate*, **23**, 3249–3281.

765 Kwon, Y., C. Deser, and C. Cassou, 2011: Coupled atmosphere–mixed layer ocean
766 response to ocean heat flux convergence along the Kuroshio Current Extension. *Climate*
767 *Dyn*., **36**, 2295–2312.
768 Kwon, Y.-O., and T. Joyce, 2013: Northern Hemisphere winter atmospheric transient
769 eddy heat fluxes and the Gulf Stream and Kuroshio-Oyashio Extension variability. *J*.
770 *Climate*, **26**, 9839-9859.
771 Liu, Z., and L. Wu, 2004: Atmospheric response to North Pacific SST: The Role of
772 Ocean-Atmosphere Coupling. *J*. *Climate*, **17**, 1859-1882.
773 Liu, Q., N. Wen, and Z. Liu, 2006: An observational study of the impact of the North
774 Pacific SST on the atmosphere. *Geophys*. *Res*. *Lett*., **33**, doi:10.1029/2006GL026082.
775 Lee, D., Z. Liu, and Y. Liu, 2008: Beyond thermal interaction between ocean and
776 atmosphere: On the extratropical climate variability due to the wind-induced SST. *J*.
777 *Climate*, **21**, 2001–2018.
778 Mantua, N.J., S.R. Hare, Y. Zhang, J.M. Wallace, and R.C. Francis, 1997: A Pacific
779 Interdecadal Climate Oscillation with Impacts on Salmon Production. *Bull*. *Amer*. *Met*.
780 *Soc*., **78**, 1069-1079.
781 Minobe, S., A. Kuwano-Yoshida, N. Komori, S. Xie, and R. Small, 2008: Influence of
782 the Gulf Stream on the troposphere. *Nature*, **452**, 206–209.
783 Minobe, S., A. Kuwano-Yoshida, M. Miyashita, H. Tokinaga, and S.-P. Xie, 2010:
784 Atmospheric Response to the Gulf Stream: Seasonal Variations. *J*. *Climate*, **23**, 3699-
785 3719.
786 Nakamura, H., T. Sampe, Y. Tanimoto, and A. Shimpo, 2004: Observed associations
787 among storm tracks, jet streams and midlatitude oceanic fronts, "Earth's Climate: The

788 Ocean-Atmosphere Interaction", C. Wang, S.-P. Xie and J. A. Carton, Eds., Geophys.
789 Monogr., **147**, American Geophysical Union, Washington, D.C., U.S.A., 329-346.
790 Nakamura, H., T. Sampe, A. Goto, W. Ohfuchi, and S.-P. Xie, 2008: On the importance
791 of mid-latitude oceanic frontal zones for the mean state and dominant variability in the
792 tropospheric circulation. *Geophys*. *Res*. *Lett*., **35**, L15709, doi:10.1029/2008GL034010.
793 Neale, R., and co-authors, 2010: Description of the NCAR community atmosphere model
794 (CAM 5.0). *NCAR Tech*. *Note*, *NCAR/TN-486+*.
795 Newman, M., G. N. Kiladis, K. M. Weickmann, F. M. Ralph, and P. D. Sardeshmukh
796 2012: Relative contributions of synoptic and low-frequency eddies to time-mean
797 atmospheric moisture transport, including the role of atmospheric rivers. *J*. *Climate*, **25**,
798 7341-7361.
799 Newman, M., 2013: An empirical benchmark for decadal forecasts of global surface
800 temperature anomalies. *J*. *Climate*, **26**, 5260-5269.
801 Nieman, S.J., 1990: A diagnosis of non-quasigeostrophic vertical motion for a model-
802 simulated rapidly intensifying marine extratropical cyclone. M.S. Thesis, Department of
803 Meteorology, University of Wisconsin-Madison, 181pp.
804 Nonaka, M. and S.-P.Xie, 2003: Covariations of SST and Wind over the Kuroshio and Its
805 Extension: Evidence for Ocean-to-Atmospheric Feedback. *J*. *Climate*, **16**, 1404-1413.
806 Nonaka, M., H. Nakamura, Y. Tanimoto, T. Kagimoto, and H. Sasaki, 2006: Decadal
807 Variability in the Kuroshio-Oyashio Extension Simulations in an Eddy-Resolving
808 OGCM. *J*. *Climate*, **19**, 1970-1989.

809 Nonaka, M., et al., 2009: Air-Sea Heat Exchanges Characteristic of a Prominent
810 Midlatitude Oceanic Front in the South Indian Ocean as Simulated in a High-Resolution
811 Coupled GCM. *J. Climate*, **22**, 6515-6535.
812 Okajima, S., H. Nakamura, K. Nishii, T. Miyasaka, A. Kuwano-Yoshida, 2014:
813 Assessing the Importance of Prominent Warm SST Anomalies over the Midlatitude
814 North Pacific in Forcing Large-Scale Atmospheric Anomalies during 2011 Summer and
815 Autumn. *J. Climate*, **27**, 3889–3903.
816 O'Reilly, C. H., and A. Czaja, 2014: The response of the Pacific storm track and
817 atmospheric circulation to Kuroshio Extension variability. *Quart. J. R. Met. Soc*, in press,
818 doi: 10.1002/qj.2334
819 Park, S., C. Deser, and M.A. Alexander, 2005: Estimation of the Surface Heat Flux
820 Response to Sea Surface Temperature Anomalies over the Global Oceans. *J. Climate*, **18**,
821 4582-4599.
822 Pauley, P.M., and S.J. Nieman, 1992: A comparison of quasigeostrophic and
823 nonquasigeostrophic vertical motions for a rapidly intensifying marine extratropical
824 cyclone. *Mon. Wea. Rev.*, **120**, 1108-1134.
825 Peng, S., W. Robinson, and M. Hoerling, 1997: The modeled atmospheric response to
826 midlatitude SST anomalies and its dependence on background circulation states. *J.*
827 *Climate*, **10**, 971–987.
828 Peng, S., and J.S. Whitaker, 1999: Mechanisms determining the atmospheric response to
829 midlatitude SST anomalies. *J. Climate,* **12,** 1393–1408.
830 Peng, S., and W. Robinson, 2001: Relationships between atmospheric internal variability
831 and the responses to an extratropical SST anomaly. *J. Climate*, **14**, 2943-2959.

832 Peng, S., W.A. Robinson, and S. Li, 2003: Mechanisms for the NAO responses to the
833 North Atlantic SST tripole. *J. Climate*, **16**, 1987-2004.
834 Pitcher, E.J., M.L. Blackmon, G.T. Bates, and S. Muñoz, 1988: The effect of North
835 Pacific sea surface temperature anomalies on the January climate of a general circulation
836 model. *J. Atmos. Sci.*, **45**, 173-188.
837 Qiu, B., 2000: Interannual variability of the Kuroshio Extension system and its impact on
838 the wintertime SST field. *J. Phys. Oceanogr.*, **30**, 1486–1502.
839 Qiu, B., N. Schneider, and S. Chen, 2007: Coupled Decadal Variability in the North
840 Pacific: An observationally constrained idealized model. *J. Climate*, **20**, 3602-3620.
841 Qiu, B., S. Chen, N. Schneider, and B. Taguchi, 2014: A coupled decadal prediction of
842 the dynamic state of the Kuroshio Extension system. *J. Climate*, **27**, 1751-1764.
843 Raisanen, J., 1995: Factors affecting synoptic-scale vertical motions: a statistical study
844 using a generalized omega equation. *Mon. Wea. Rev.*, **123**, 2447-2460.
845 Renard, R.J., and L.C. Clarke, 1965: Experiments in numerical objective frontal analysis.
846 *Mon. Wea. Rev.*, **93,** 547-556.
847 Sardeshmukh, P.D. and B.J. Hoskins, 1988: The generation of global rotational flow by
848 steady idealized tropical divergence. *J. Atmos. Sci.*, **45**, 1228-1251.
849 Saulière, J., D. J. Brayshaw, B. Hoskins, M. Blackburn, 2012: Further Investigation of
850 the Impact of Idealized Continents and SST Distributions on the Northern Hemisphere
851 Storm Tracks. *J. Atmos. Sci.*, **69**, 840–856.
852 Sasaki, Y.N., S. Minobe, T. Asai, and M. Inatsu, 2012: Influence of the Kuroshio in the
853 East China Sea on the Early Summer (Baiu) Rain. *J. Climate*, **25**, 6627-6645.

854 Schneider, N., and A. J. Miller, 2001: Predicting Western North Pacific Ocean Climate.
855 *J. Climate*, **14**, 3997-4002.
856 Schneider, N., and B.D. Cornuelle, 2005: The forcing of the Pacific Decadal Oscillation.
857 *J. Climate*, **18**, 4355-4373.
858 Seo, H., Y.-O. Kwon, and J.-J. Park, 2014: On the effect of marginal sea SST variability
859 on the North Pacific atmospheric circulation. *J. Geophys. Res. Atmos.*, **119**, DOI:
860 10.1002/2013JD020523.
861 Sheldon, L., and A. Czaja, 2014: Seasonal and interannual variability of an index of deep
862 atmospheric convection over the western boundary currents. *Quart. J. R. Met. Soc.*, **140**,
863 22-30.
864 Small, R., and co-authors, 2008: Air–sea interaction over ocean fronts and eddies. *Dyn.*
865 *Atmos. Oceans*, **45**, 274–319.
866 Small, R.J., R.A. Tomas, and F.O. Bryan, 2013: Storm track response to ocean fronts in a
867 global high-resolution climate model. *Clim. Dyn.*, 1-24.
868 Smirnov, D., and D. J. Vimont, 2012: Extratropical forcing of tropical Atlantic variability
869 during boreal summer and fall. *J. Climate*, **25**, 2056-2076.
870 Smirnov, D., M. Newman and M.A. Alexander, 2014: Investigating the role of ocean-
871 atmosphere coupling in the North Pacific Ocean. *J. Climate*, **27**, 592-606.
872 Taguchi, B., H, Nakamura, M. Nonaka, and S.-P. Xie, 2009: Influences of the
873 Kuroshio/Oyashio Extensions on Air-Sea Heat Exchanges and Storm-Track Activity as
874 Revealed in Regional Atmospheric Model Simulations for the 2003/04 Cold Season. *J.*
875 *Climate*, **22**, 6536-6560.

876 Taguchi, B., H. Nakamura, M. Nonaka, N. Komori, A. Kuwano-Yoshida, K. Takaya, and
877 A. Goto, 2012: Seasonal evolutions of atmospheric response to decadal SST anomalies in
878 the North Pacific subarctic frontal zone: Observations and a coupled model simulation. *J*.
879 *Climate*, **25**, 111–139.
880 Ting, M., 1991: The Stationary Wave Response to a Midlatitude SST Anomaly in an
881 Idealized GCM. *J*. *Climate*, **48**, 1249-1275.
882 Trenberth, K.E., 1978: On the interpretation of the diagnostic quasi-geostrophic omega
883 equation. *Mon*. *Wea*. *Rev*., **106**, 131-137.
884 Uppala, S., D. Dee, S. Kobayashi, P. Berrisford, and A. Simmons (2008): Towards a
885 climate data assimilation system: Status update of ERA-Interim, in ECMWF Newsletter,
886 115, pp. 12–18, European Centre for Medium-Range Weather Forecasts, Reading, UK.
887 (Available at http://www.ecmwf.int/publications/newsletters).
888 Watanabe, M., Jin, F., and L. Pan, 2006: Accelerated Iterative Method for Solving Steady
889 Problems of Linearized Atmospheric Models. *J*. *Atmos*. *Sci*., **63**, 3366–3382.
890 Wehner, M. F and co-authors, 2014: The effect of horizontal resolution on simulation
891 quality in the Community Atmospheric Model, CAM5.1. Submitted to the *Journal of*
892 *Modeling the Earth System*.
893 Willison, J., W.A. Robinson, and G.M. Lackmann, 2013: The Importance of Resolving
894 Mesoscale Latent Heating in the North Atlantic Storm Track. *J. Atmos. Sci.*, **70**, 2234-
895 2250.
896 Woollings, T., B. Hoskins, M. Blackburn, D. Hassell, and K. Hodges, 2010: Storm track
897 sensitivity to sea surface temperature resolution in a regional atmosphere model. *Climate*
898 *Dynamics*, **35**, 341-353.

899 Xu, H., M. Xu, S.-P. Xie, and Y. Wang, 2011: Deep Atmospheric Response to the Spring
900 Kuroshio over the East China Sea. *J*. *Climate*, **24**, 4959-4972.
901 Yu, L., and R. Weller, 2007: Objectively analyzed air–sea heat fluxes for the global ice-
902 free oceans (1981–2005). *Bull*. *Amer*. *Meteor*. *Soc*., **88**, 527–539.
903 Yulaeva, E., N. Schneider, D. Pierce, and T. Barnett, 2001: Mod- eling of North Pacific
904 climate variability forced by oceanic heat flux anomalies. J. Climate, 14, 4027–4046.
905

906 Figure captions

907 Figure 1: (a) Nov-Mar OEI SST regression and (b) after multiplying (a) by 3, then
908 smoothing and applying cosine-taper filter (see text). (c) Scatter of point by point -
909 1*dSST/dy from 145°E to 165°E as a function of latitude (dots) for the warm (red,
910 northward Oyashio shift) and cold (blue) experiments. The black box shown in (b) shows
911 the region used for "across-front" zonal averages (145°-165°E) in subsequent figures.
912
913 Figure 2: Standardized POEI3 (color) based on the 1° OAFlux SST dataset, 1958-2012
914 and OEI (without trend removal) from Frankignoul et al. (2011; black line) from 1982-
915 2012.
916
917 Figure 3: (a) Mean response (contour, c.i. $4x10^{-7}$ s^{-1}) of the Dec-Mar across-front (145-
918 165°E) divergence in the HR simulation. Gray shading encloses areas significant at the
919 95% confidence level. (b) Evolution of the 5-day running mean response of across-front
920 divergence. Thick (thin) line indicates the response pattern r.m.s. (pattern correlation)
921 with the equilibrium pattern in (a). The r.m.s. is normalized to unity by the day 3 value.
922
923 Figure 4: The mean December-March atmospheric response (warm-cold) to a shift in the
924 Oyashio Extension SST front in (left column) HR and (right column) LR simulations.
925 (a,b) Turbulent heat flux (color) and 950 hPa wind (vectors). Black bold vectors are
926 significant at the 95% confidence level. (c,d) Zonally averaged (145°-165°E) across-front
927 [v, ω] circulation (vectors) and θ_E (color). Black vectors are significant at the 90 %
928 confidence level. The ω component is multiplied by 2000 to aid in visualization. (e,f) 850

929 hPa $\overline{v'\theta_E'}$ (color) where stippling denotes regions significant at the 95 % confidence
930 level. The black contours indicate the mean climatological $\overline{v'\theta_E'}$. In all panels, the mean
931 difference is divided by 2.5 to account for a ±1.25σ POEI SST anomaly.
932
933 Figure 5: The contribution of the (a) total sub-monthly 850 hPa $\overline{v'T'}$ separated into the (b)
934 2-6 day bandpass and (c) 6-30 day bandpass components in the HR simulation. Black
935 dots denote regions that are significant at the 95% confidence level. Note that daily
936 specific humidity output was not saved, precluding the same analysis on $\overline{v'\theta_E'}$.
937
938 Figure 6: Across-front mean December-March response (color) of (a,b) $\overline{v'\theta_E'}$ (c.i. 0.8 K
939 m s^{-1}) and (c,d) $\overline{v'v'}$ (c.i., 2 m^2 s^{-2}) in the (left) HR and (right) LR simulations. Stippling
940 denotes areas that are significant at the 95% confidence level. Thick black contours show
941 the climatological values from the HR (a,c) and LR (b,d) control simulations.
942
943 Figure 7: (a-d) Composites of anomalous SLP (contour) and high-pass filtered 850 hPa
944 $v'T'$ on days where the thermal front parameter (see text for additional information)
945 exceeds 0.15 K $(100\ km)^{-2}$ for the (a) warm, and (c) cold HR simulations and (b) warm
946 and (d) cold LR simulations. (e and f) Differences of (a) – (c) and (b) – (d), respectively.
947 In (e) and (f), thick contour encloses areas that exceed the 95% significance based on a
948 1000 sample Monte Carlo test. Note that SLP does not show up in (e,f) because it does
949 not meet the 95% significance threshold (or even the 90%).
950

951 Figure 8: Mean Dec-Mar response in (a,b) total (convective + stratiform) precipitation,
952 and (c,d) column integrated precipitable water in the (a,c) HR and (b,d) LR simulations.
953 Contours enclose areas that are significant at the 95% confidence level.
954
955 Figure 9: Snapshot of frontal passage from November 4th of ensemble member #2. (a – d)
956 Daily mean SLP (contours; c.i. 4 hPa) and total precipitation (mm day^{-1}) for the warm
957 and cold simulations of HR and LR. (e,f) Difference between (a,c) and (b,d),
958 respectively. Contour interval for SLP is 1 hPa, negative contours are dashed and zero
959 contour is omitted.
960
961 Figure 10: Across-front Dec-Mar mean difference of terms comprising the
962 thermodynamic budget for the (a,c,e) HR and (b,d,f) LR simulations. (a, b) Sum of all
963 horizontal terms [I-IV] in (1), (c,d) sum of all vertical terms [V-VI], and (e,f) diabatic
964 heating (colors) and their Laplacian (contours). Thin dotted lines show the approximate
965 latitudinal position of the positive SST anomaly, and are used for meridional averaging in
966 Fig. 11.
967
968 Figure 11: Vertical profiles of the heating rate response (K day^{-1}) arising from (a)
969 horizontal (blue), vertical (gray) transport and diabatic processes (red). (b and c)
970 separation of the horizontal component from (a) into mean (solid) and eddy (dash)
971 components for (b) zonal and (c) meridional transport. (d) Separation of vertical
972 component in (a) into mean and eddy terms. The thick (thin) lines are for HR (LR). Note
973 the different x-axis scale in (b-d) compared to (a).
974

975 Figure 12: (a and b) Across-front mean ω^R (contour) and ω - ω^R (red: positive; blue:
976 negative) for the (a) HR and (b) LR simulations. Contour interval is 0.005 Pa s^{-1}. The
977 contribution to ω^R decomposed into the (c,d) mean thermal, (e,f) diabatic heating
978 components for the (left column) HR and (right column) LR simulations. The eddy
979 thermal, mean vorticity and eddy vorticity components are negligible (less than one
980 contour) and not shown. See (2) for terms.
981
982 Figure 13: (a) Mean thermal contribution to across front ω^R response in the HR
983 simulation (same as Fig. 12c but with c.i. 0.0025 Pa s^{-1}). (b) Same as (a) but setting [U,
984 V] to climatological values from the HR control simulations. (c) Same as (a) but setting T
985 set to climatological values. (d) Same as (c) but also setting U to climatological values.
986 (e) Same as (c) but also setting V to climatological values.
987
988 Figure 14: Observational counterpart to Fig. 4 based on (left) simultaneous and (right)
989 14-day lagged (right) regressions of the ERAI atmospheric variables on the daily POEI.
990
991 Figure 15: Mean Dec-Mar difference in (a,b) 800 hPa θ_E and (c,d) 300 hPa geopotential
992 height over the North Pacific for the (a,c) HR and (b,d) LR simulations. Black contour
993 denotes areas significant at the 95% confidence level based on a Student's t-test.
994

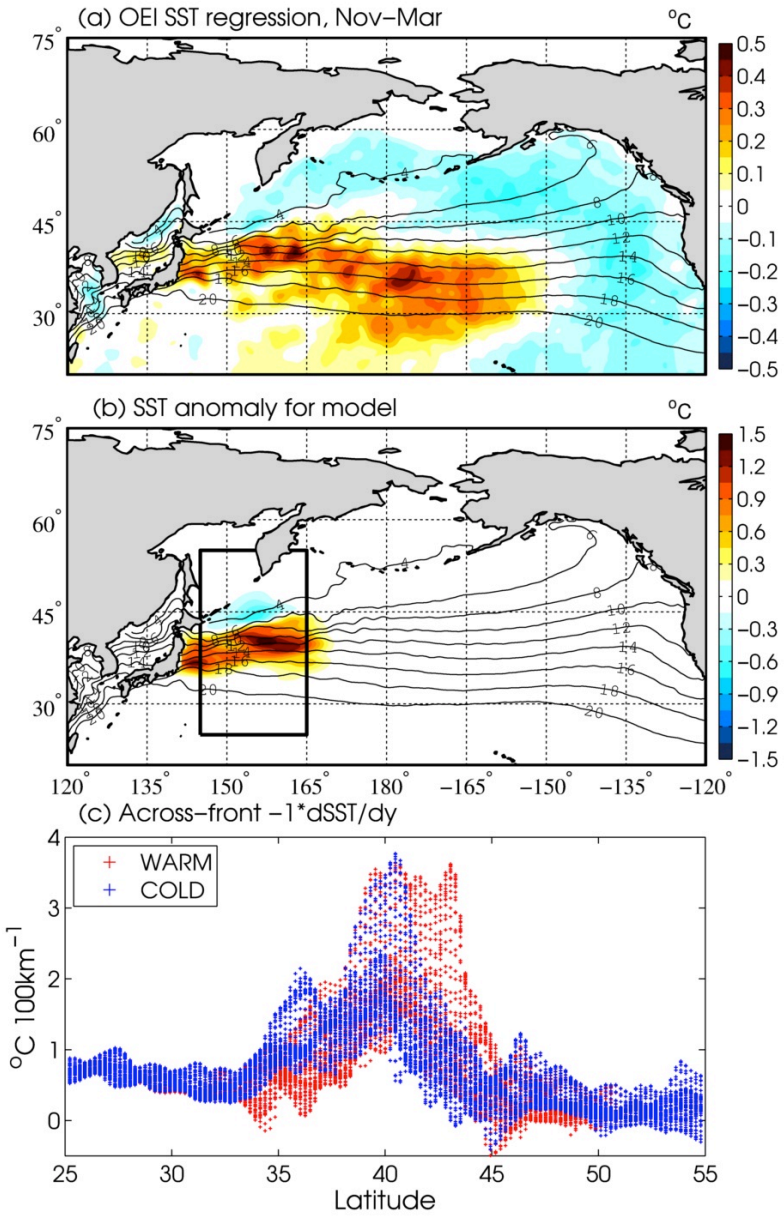

Figure 1: (a) Nov-Mar OEI SST regression and (b) after multiplying (a) by 3, then smoothing and applying cosine-taper filter (see text). (c) Scatter of point by point -1*dSST/dy from 145°E to 165°E as a function of latitude (dots) for the warm (red, northward Oyashio shift) and cold (blue) experiments. The black box shown in (b) shows the region used for "across-front" zonal averages (145°-165°E) in subsequent figures.

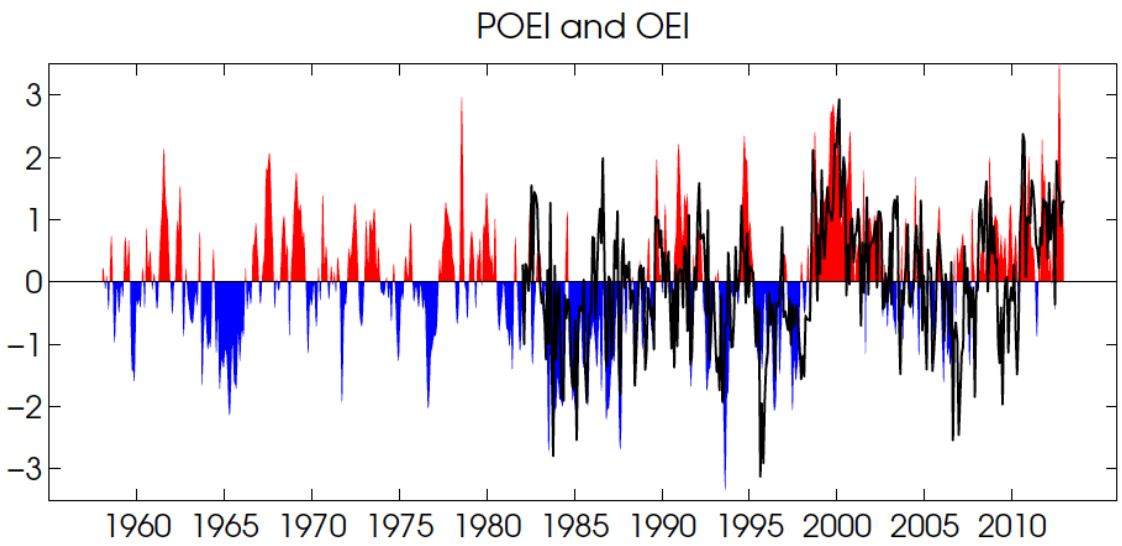

Figure 2: Standardized POEI3 (color) based on the 1° OAFlux SST dataset, 1958-2012 and non-detrended OEI from Frankignoul et al. (2011; black line) from 1982-2012.

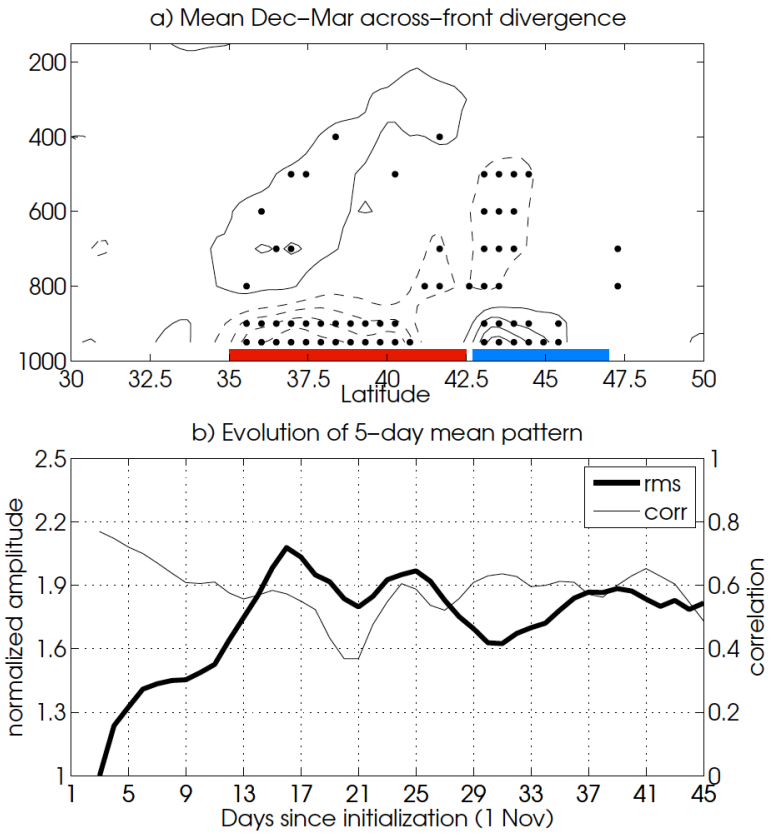

Figure 3: (a) Mean response (contour, c.i. 4×10^{-7} s^{-1}) of the Dec-Mar across-front (145-165°E) divergence in the HR simulation. Black dots denote grid points significant at the 95% confidence level. Red (blue) shading denotes the region of the positive (negative) SST anomaly. (b) Evolution of the 5-day running mean response of across-front divergence. Thick (thin) line indicates the response pattern r.m.s. (pattern correlation) with the equilibrium pattern in (a). The r.m.s. is normalized to unity by the day 3 value.

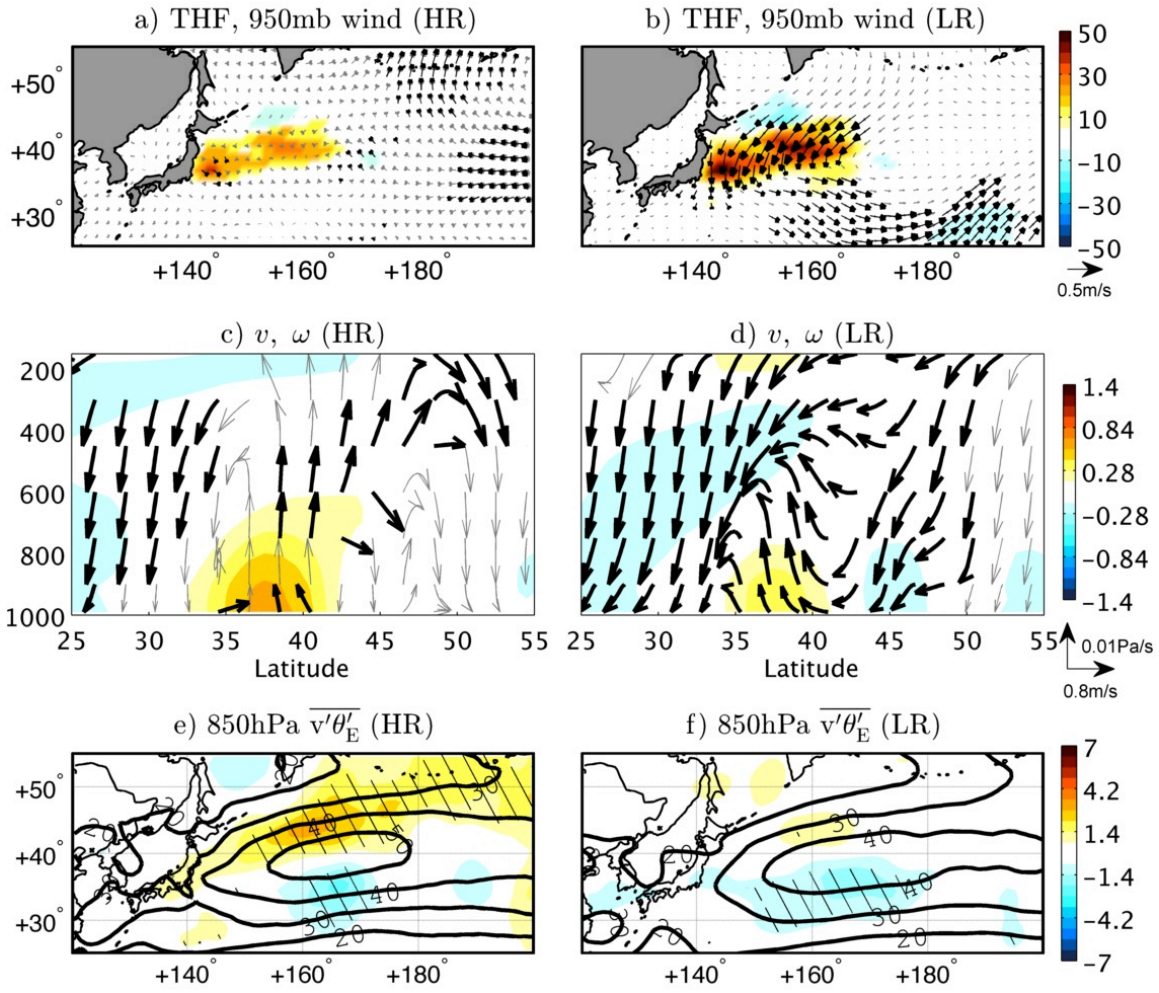

Figure 4: The mean December-March atmospheric response (warm-cold) to a shift in the Oyashio Extension SST front in (left column) HR and (right column) LR simulations. (a,b) Turbulent heat flux (color) and 950 hPa wind (vectors). Black bold vectors are significant at the 95% confidence level. (c,d) Zonally averaged (145°-165°E) across-front [v, ω] circulation (vectors) and θ_E (color). Black vectors are significant at the 90 % confidence level. The ω component is multiplied by 2000 to aid in visualization. (e,f) 850 hPa $\overline{v'\theta_E'}$ (color) where stippling denotes regions significant at the 95 % confidence level. The black contours indicate the mean climatological $\overline{v'\theta_E'}$. In all panels, the mean difference is divided by 2.5 to account for a ±1.25σ POEI SST anomaly.

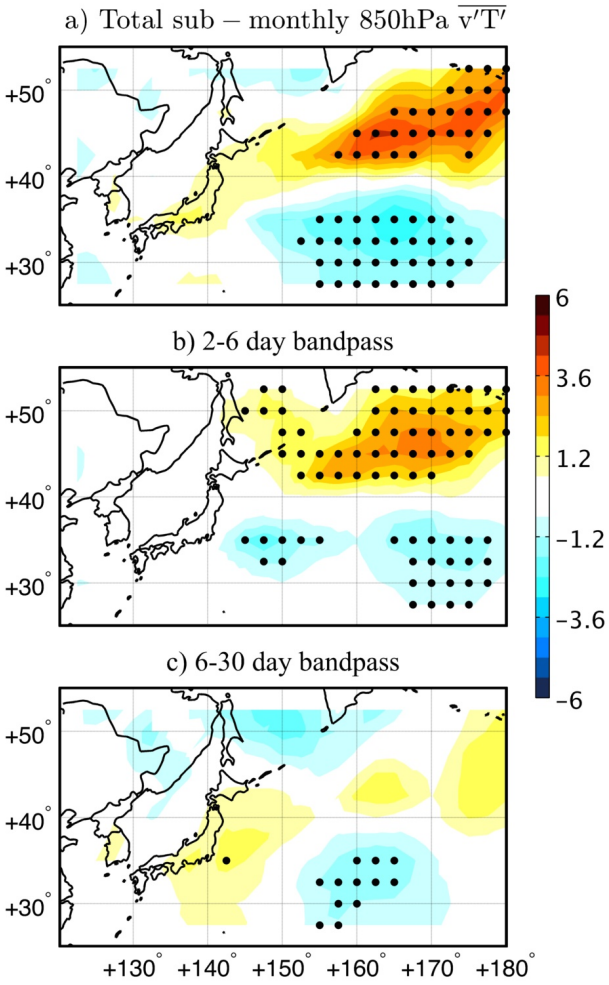

Figure 5: The contribution of the (a) total sub-monthly 850 hPa $\overline{v'T'}$ separated into the (b) 2-6 day bandpass and (c) 6-30 day bandpass components in the HR simulation. Black dots denote regions that are significant at the 95% confidence level. Note that daily specific humidity output was not saved, precluding the same analysis on $\overline{v'\theta_E{}'}$.

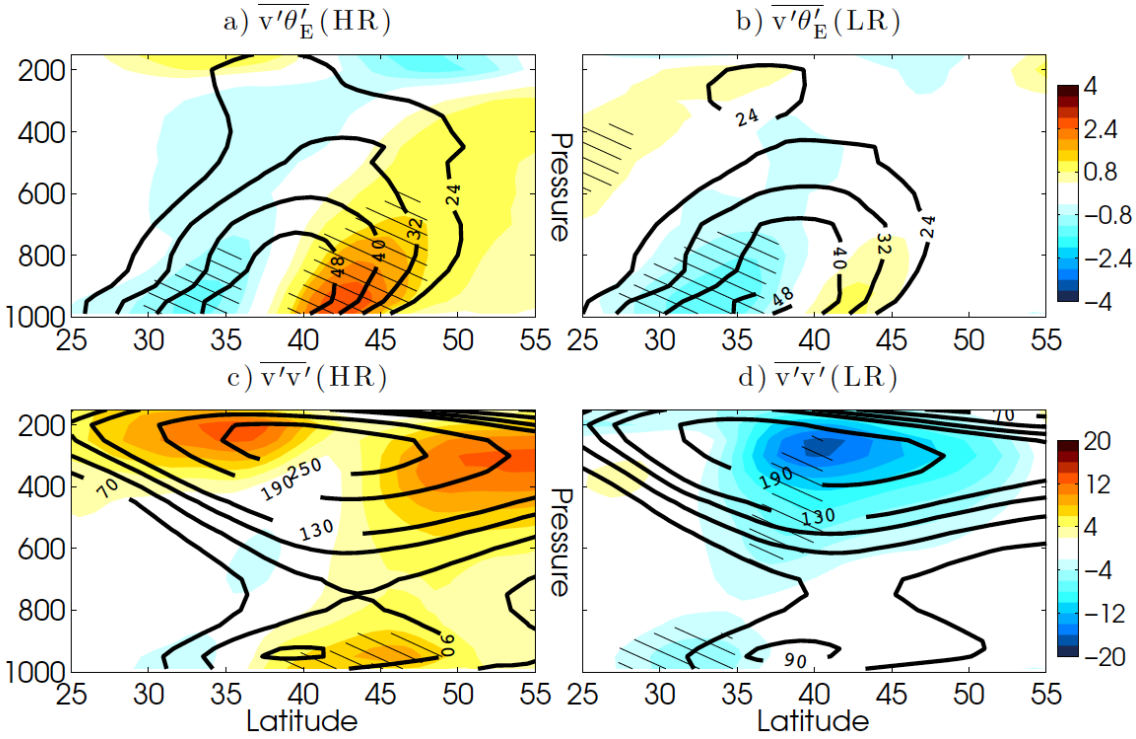

Figure 6: Across-front mean December-March response (color) of (a,b) $\overline{v'\theta_E'}$ (c.i. 0.8 K m s^{-1}) and (c,d) $\overline{v'v'}$ (c.i., 2 m^2 s^{-2}) in the (left) HR and (right) LR simulations. Stippling denotes areas that are significant at the 95% confidence level. Thick black contours show the climatological values from the HR (a,c) and LR (b,d) control simulations.

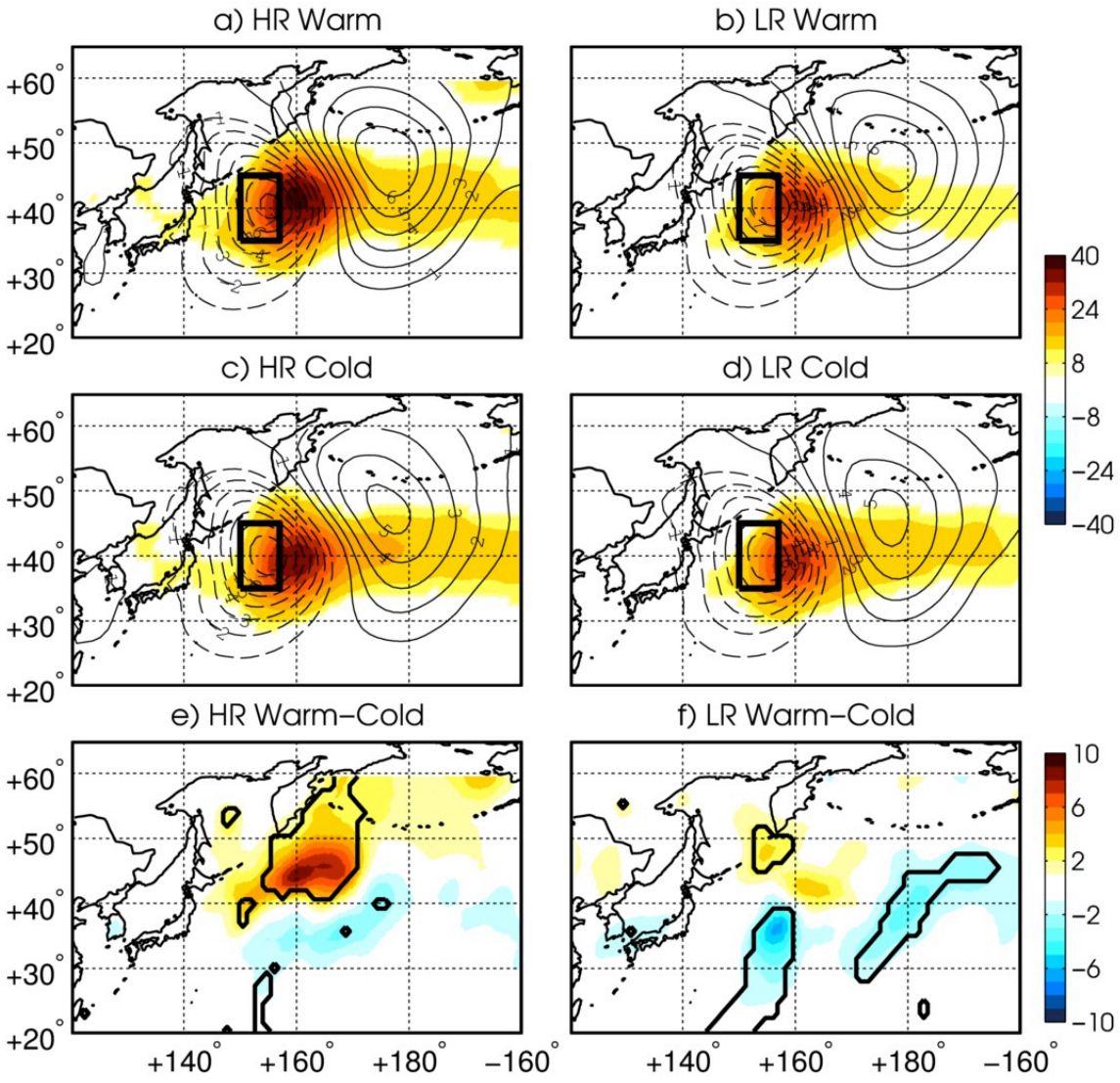

Figure 7: (a-d) Composites of anomalous SLP (contour) and high-pass filtered 850 hPa $v'T'$ on days where the thermal front parameter (see text for additional information) exceeds 0.15 K (100 km)$^{-2}$ for the (a) warm, and (c) cold HR simulations and (b) warm and (d) cold LR simulations. (e and f) Differences of (a) – (c) and (b) – (d), respectively. In (e) and (f), thick contour encloses areas that exceed the 95% significance based on a 1000 sample Monte Carlo test. Note that SLP does not show up in (e,f) because it does not meet the 95% significance threshold (or even the 90%).

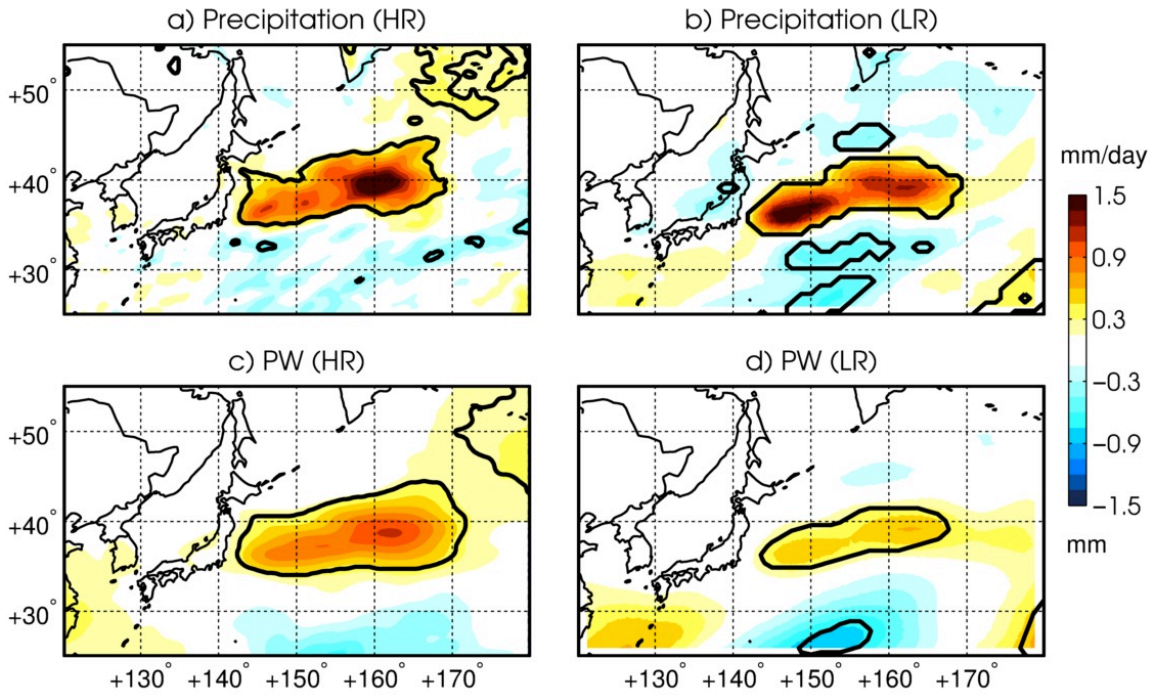

Figure 8: Mean Dec-Mar response in (a,b) total (convective + stratiform) precipitation, and (c,d) column integrated precipitable water in the (a,c) HR and (b,d) LR simulations. Contours enclose areas that are significant at the 95% confidence level.

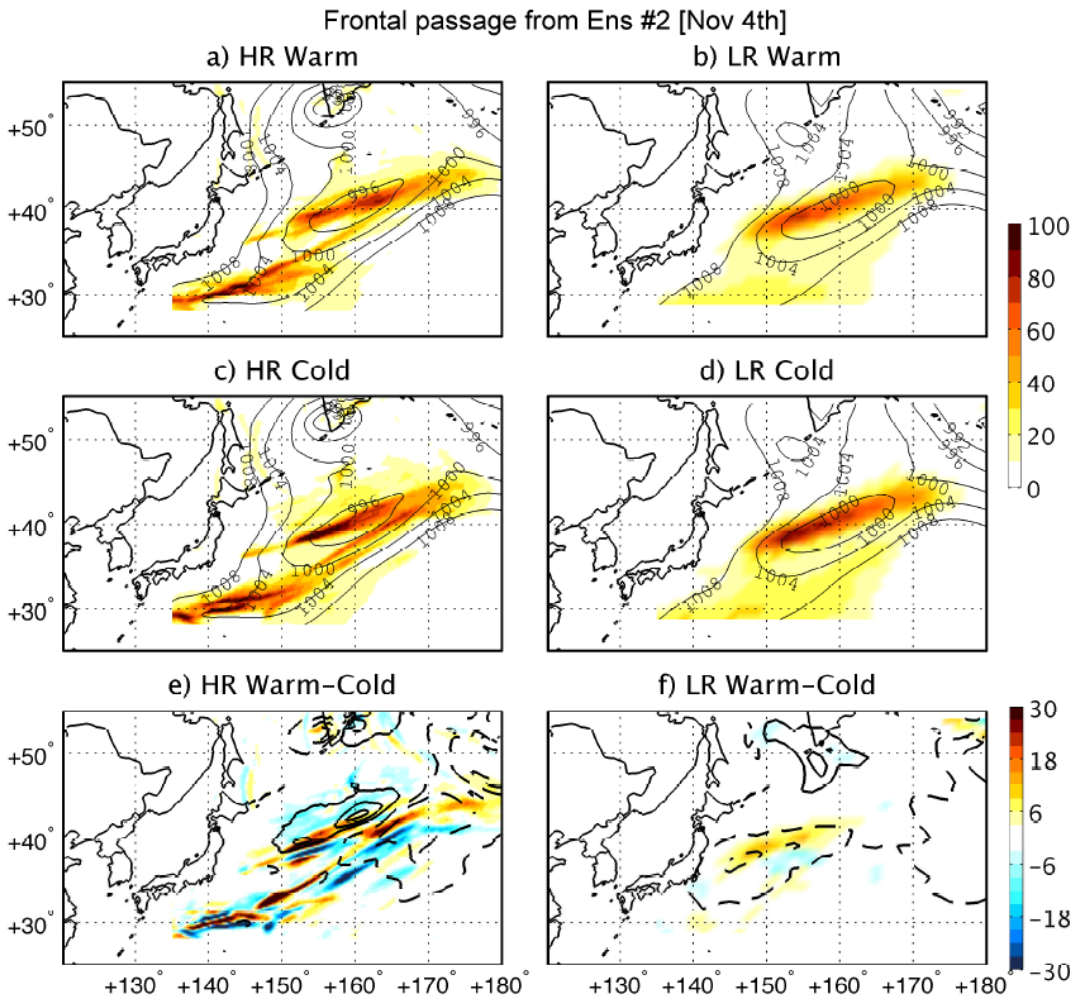

Figure 9: Snapshot of frontal passage from November 4th of ensemble member #2. (a – d) Daily mean SLP (contours; c.i. 4 hPa) and total precipitation (mm day^{-1}) for the warm and cold simulations of HR and LR. (e,f) Difference between (a,c) and (b,d), respectively. Contour interval for SLP is 1 hPa, negative contours are dashed and zero contour is omitted.

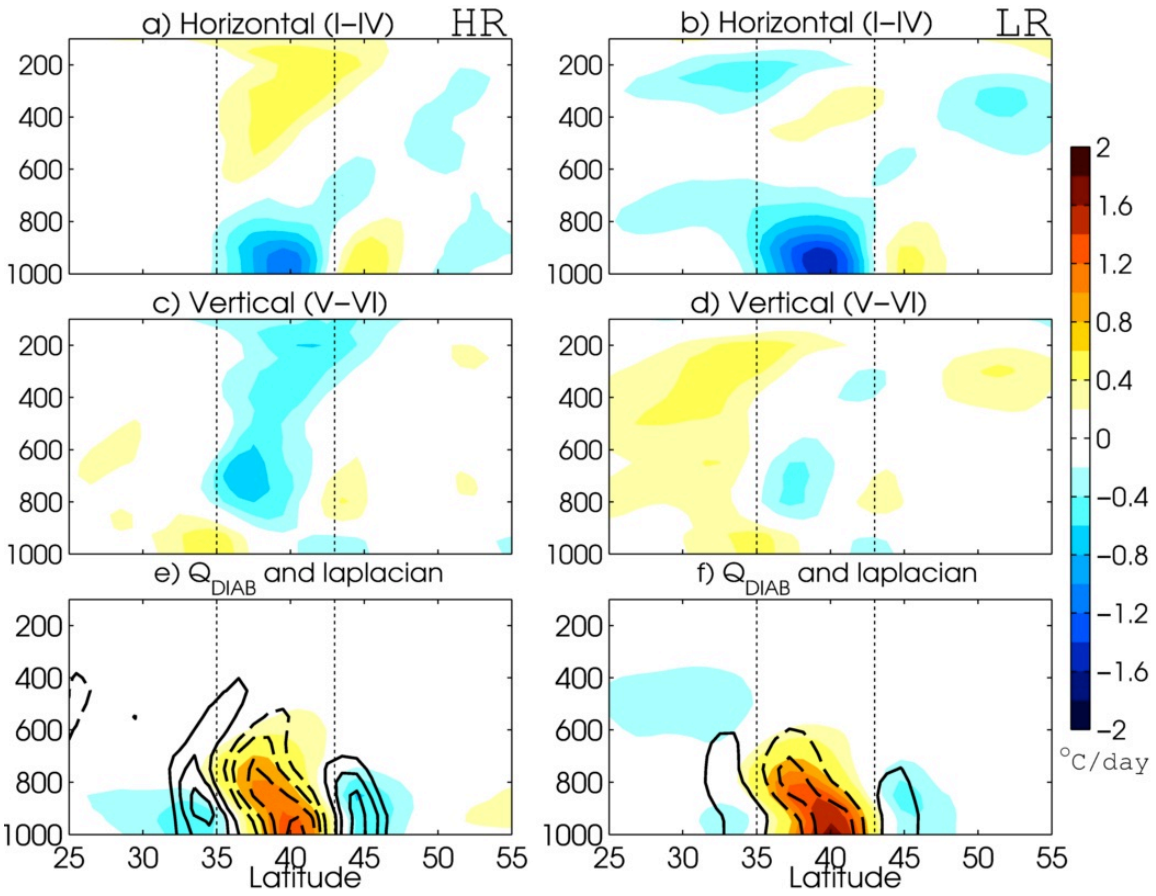

Figure 10: Across-front Dec-Mar mean difference of terms comprising the thermodynamic budget for the (a,c,e) HR and (b,d,f) LR simulations. (a, b) Sum of all horizontal terms [I-IV] in (1), (c,d) sum of all vertical terms [V-VI], and (e,f) diabatic heating (colors) and their Laplacian (contours). Thin dotted lines show the approximate latitudinal position of the positive SST anomaly, and are used for meridional averaging in Fig. 11.

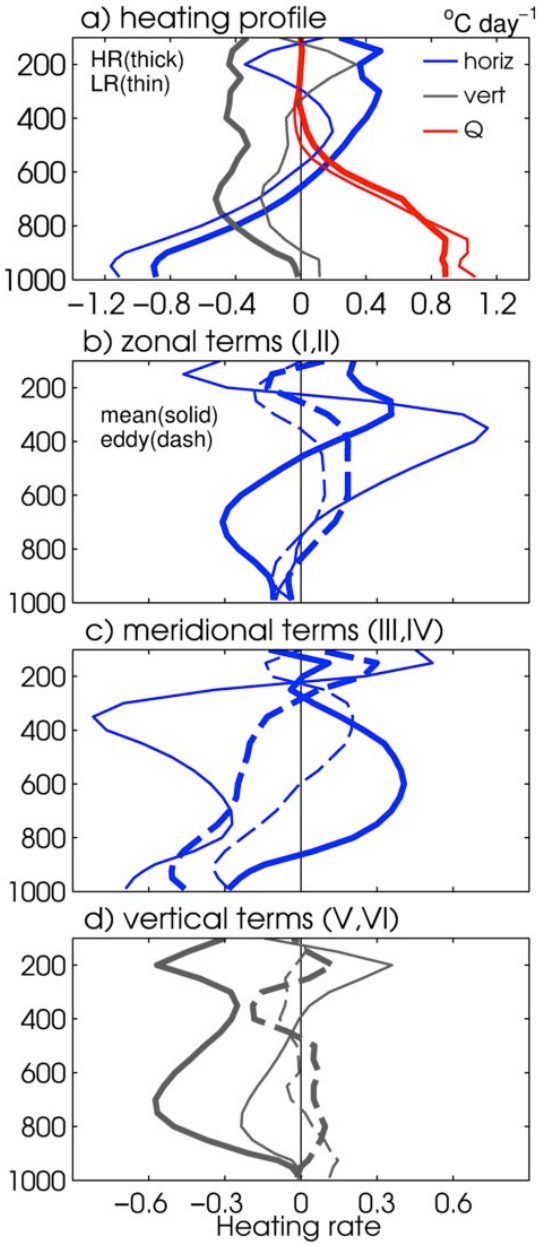

Figure 11: Vertical profiles of the heating rate response (K day^{-1}) arising from (a) horizontal (blue), vertical (gray) transport and diabatic processes (red). (b and c) separation of the horizontal component from (a) into mean (solid) and eddy (dash) components for (b) zonal and (c) meridional transport. (d) Separation of vertical component in (a) into mean and eddy terms. The thick (thin) lines are for HR (LR). Note the different x-axis scale in (b-d) compared to (a).

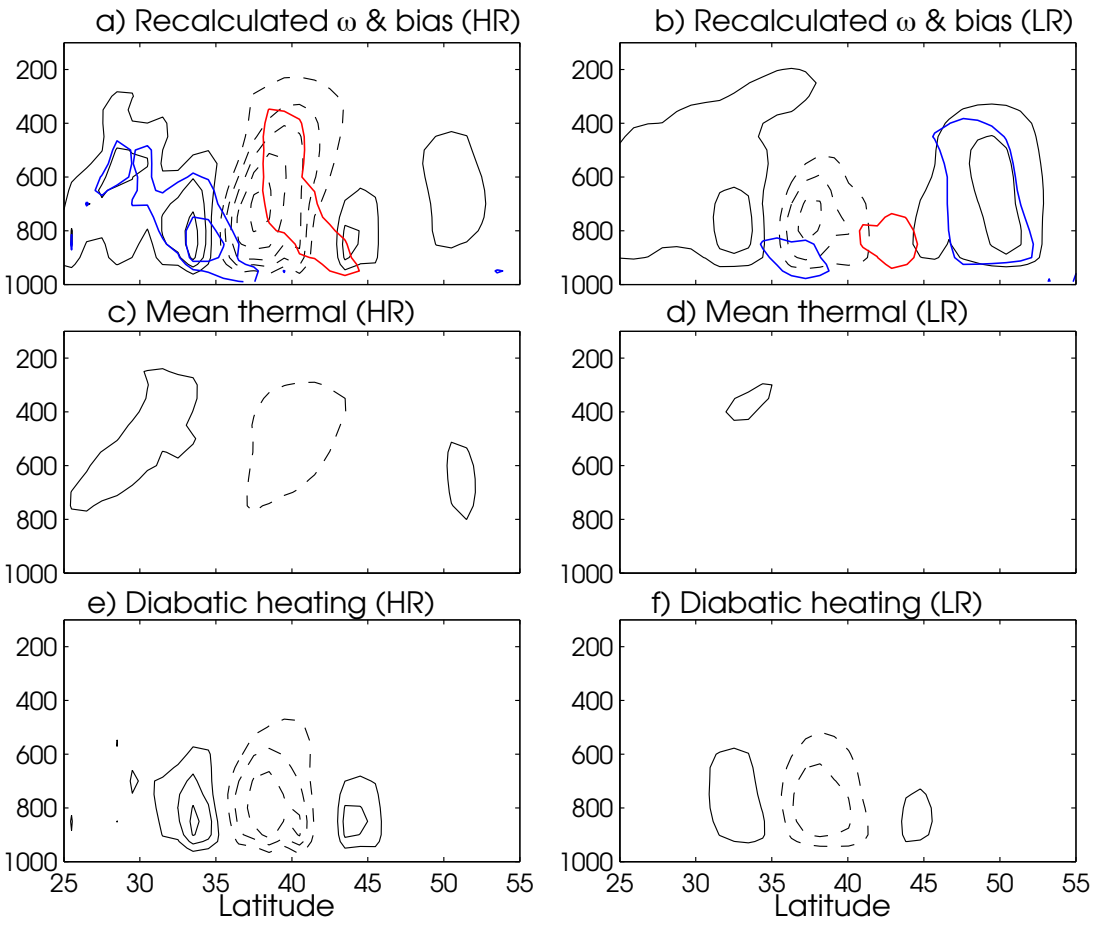

Figure 12: (a and b) Across-front mean ω^R (contour) and ω - ω^R (red: positive; blue: negative) for the (a) HR and (b) LR simulations. Contour interval is 0.005 Pa s^{-1}. The contribution to ω^R decomposed into the (c,d) mean thermal, (e,f) diabatic heating components for the (left column) HR and (right column) LR simulations. The eddy thermal, mean vorticity and eddy vorticity components are negligible (less than one contour) and not shown. See (2) for terms.

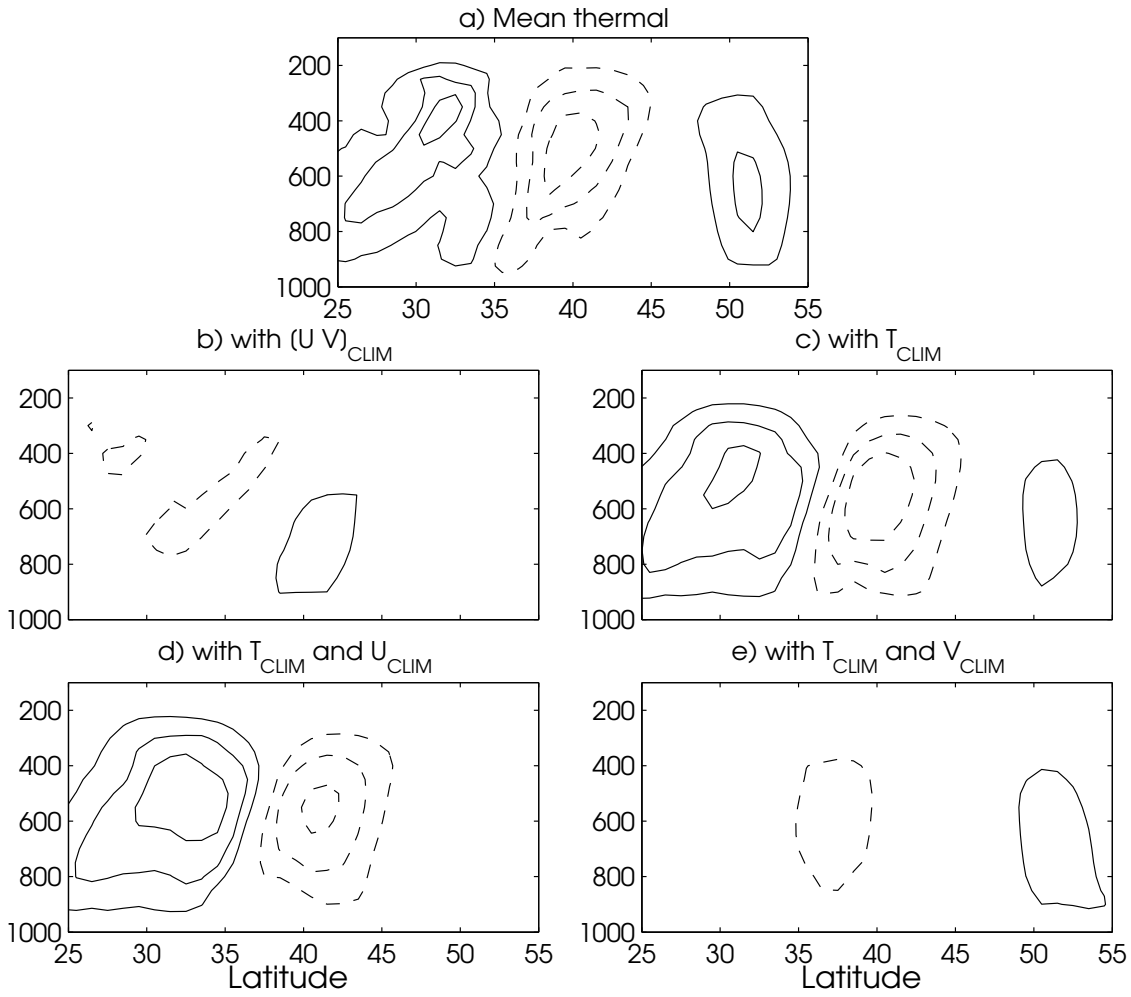

Figure 13: (a) Mean thermal contribution to across front ω^R response in the HR simulation (same as Fig. 12c but with c.i. 0.0025 Pa s^{-1}). (b) Same as (a) but setting [U, V] to climatological values from the HR control simulations. (c) Same as (a) but setting T set to climatological values. (d) Same as (c) but also setting U to climatological values. (e) Same as (c) but also setting V to climatological values.

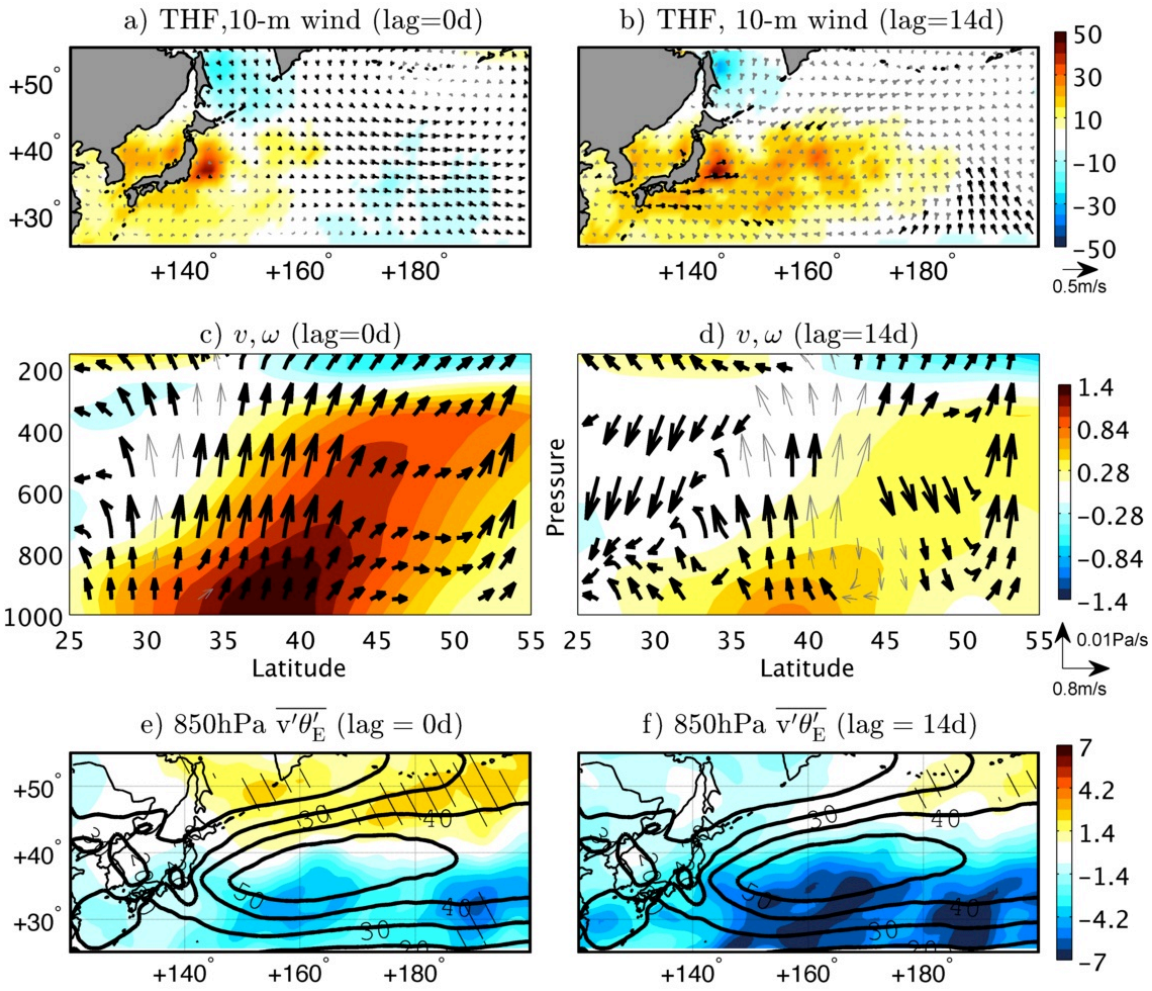

Figure 14: Observational counterpart to Fig. 4 based on (left) simultaneous and (right) 14-day lagged (right) regressions of the ERAI atmospheric variables on the daily POEI.

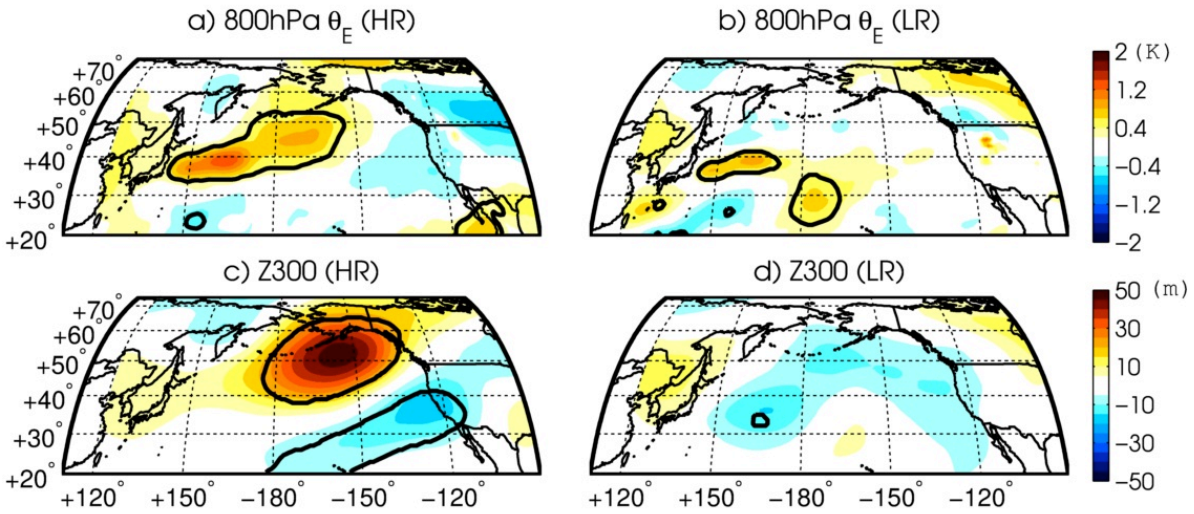

Figure 15: Mean Dec-Mar difference in (a,b) 800 hPa θ_E and (c,d) 300 hPa geopotential height over the North Pacific for the (a,c) HR and (b,d) LR simulations. Black contour denotes areas significant at the 95% confidence level based on a Student's t-test.